EFFECT OF SURFACES ON STRENGTH EVOLUTION OF SILICON NANOSTRUCTURES

A Dissertation

Presented to the Faculty of the Graduate School

of Cornell University

in Partial Fulfillment of the Requirements for the Degree of

Doctor of Philosophy

by

Scott Joseph Grutzik

August 2015

EFFECT OF SURFACES ON STRENGTH EVOLUTION OF SILICON NANOSTRUCTURES

Scott Joseph Grutzik, Ph.D.

Cornell University 2015

Previous experiments have shown a link between oxidation and strength changes in single crystal silicon nanostructures but provided no clues as to the mechanisms leading to this relationship. Through a mix of atomic force microscope based fracture strength experiments, molecular dynamics modeling, and comparisons to past experiments we have show that the previously described strength decrease is a result of oxidation induced roughening of an initially flat silicon (1 1 1) surface and that this effect is transient. In a fully developed native oxide the Si-SiO_2 interface flattens. As a result the strength recovers with some indication that it becomes slightly stronger than in its initially hydrogen terminated state. Experimental results are corroborated by Brad Boyce at Sandia National Laboratories using a completely separate line of testing involving micro-scale, polysilicon devices and the slack chain method. In addition, we demonstrate improvements to the calibration of the strength testing procedure, justify constitutive assumptions, and reduce overall uncertainty. Finally, we make an effort to extend the previous study of the effect of methyl monolayers on strength evolution of Si nanostructures by looking at more coating materials and longer time scales.

BIOGRAPHICAL SKETCH

Scott was born on September 12, 1987 in Wausau, WI. During high school, he was involved with various math and science related extracurricular activities, alpine ski racing, played in the high school concert and jazz bands, and was active in boy scouts, eventually receiving his Eagle Scout rank. He completed his Bachelor of Science degree at the University of Wisconsin – Madison with a dual major in Engineering Physics and Physics in 2010. He then moved to Ithaca, NY to pursue a Ph.D. in Theoretical and Applied Mechanics at Cornell University. He and his wife, Michelle, have two children. Henry was born in April of 2013 and Calvin in June of 2015.

This work is dedicated to my wife, Michelle, and children, Henry and Calvin, who continually supported me through the ups and downs that come with the life of a graduate student.

ACKNOWLEDGEMENTS

Thank you to my advisor, Alan Zehnder, for his continuous and valuable guidance. Thank you also to our collaborator Melissa Hines and her student Anqi Song for lending their expertise in silicon etching and surface chemistry. I would also like to thank Brad Boyce of Sandia National Laboratories for sharing his Si strength data. Finally, thank you to Robert Cook, Richard Gates, Brian Bush, Frank DelRio, Yvonne Gerbig, and Douglass Smith of the Nanomechanical Properties group at the National Institute for Standards and Technology for their valuable help in reference cantilever calibration and SAM deposition.

TABLE OF CONTENTS

LIST OF TABLES

LIST OF FIGURES

CHAPTER 1

INTRODUCTION

1.1 Motivation

Micro- and nanoelectromechanical systems (MEMS and NEMS) play an increasing role in many fields such as telecommunications[1], defense[2], energy harvesting [3], and biomedical devices[4]. These systems can be subjected to sustained loads, oscillating loads, dynamic shock loading, or a combination of all three. In addition to these difficult loading conditions, the small size of these devices make accurate predictions and measurements of strength and durability difficult. As a result they may be designed with overly large factors of safety with respect to mechanical failure. More efficient design will require accurate knowledge of the stochastic nature of fracture at these length scales.

For a variety of reasons, it is difficult to extrapolate macroscale material failure behavior down to the length scales required for MEMS and NEMS design. Components of these systems are often small enough that they contain few or no defects other than those introduced during processing. Also, because of their high surface to volume ratio, surface properties tend to play a larger role than volumetric properties. Nonetheless, it is possible to make some general predictions. From a continuum mechanics perspective, a smoother surface should give rise to a stronger structure. Any pit or roughness feature on the surface will act as a stress concentrator under loading and act as a potential nucleation point for fracture. In addition, oxidation of the surface or deposition of other materials can place the silicon near the surface under state of either compressive or tensile stress. It would be expected that a compressive stress would have to be overcome in order

to initiate or propagate cracks, effectively making the structure stronger, while a tensile surface stress would have the opposite effect.

1.2 Previous results

In order to provide accurate micro- and nanoscale strength data, a number of methods of material testing have been proposed. Accurate measurement of mechanical properties such as stiffness or fracture strength of micro- and nanoscale specimens is difficult. The small sizes and force involved at these length scales introduce difficulties at every step of the process. Namazu *et al.* [5] developed a nanoscale specimen that can be tested in thee point bending using an atomic force microscope (AFM). Tsuchiya *et al.* [6] developed a piezoelectrically actuated microscale, polysilicon specimen. Boyce [7] demonstrated the effect of surface flaws on strength using a high throughput method involving a slack chain of microscale, polysilicon specimens. Gaither *et al.* [8] developed a microscale, single crystal Si specimen in a Θ shaped geometry that can be loaded using a NIST calibrated nanoindenter. Stan *et al.* [9, 10] used an AFM as probe to deform synthesized Si nanowires lying on a substrate and calculated strength from the deformed shape just before failure. These methods span quite a range of testing methods, complexity, and specimen geometries. One common theme however is the effect of surface features on strength. DelRio, *et al.* [11] give an excellent review of these methods and the various factors affecting strength of nano- and microscale silicon devices.

In order to directly address the effect of surface characteristics on strength of nanoscale Si structures Alan *et al.* [12, 13] proposed an AFM based testing method using specimens similar to that of Namazu *et al.* [5] except with altered geometry to

avoid stress concentrations where the specimen attaches the bulk substrate. They were able to show that even roughness as small as 2 nm can have a significant effect on strength. They also showed a correlation between oxidation of a (1 1 1) Si surface and a decrease in strength. This work focuses on an effort to better understand the relation between oxidation and strength change. This involves studying the physical mechanisms by which oxidation affects strength (see Chapter 6) as well as observing strength trends over a longer period of time than in previous work and using a variety of surface coatings to prevent oxidation (see Chapter 7)

Chapter 2 outlines the AFM based strength testing methods used in this work, the process to convert the AFM data to a fracture strength, the stochastic failure analysis used to interpret the data, and the uncertainty quantification. Chapter 3 outlines an improvement to the AFM cantilever calibration method used in previous works that results in greatly reduced uncertainty. Chapter 4 justifies the use of a linear constitutive relation even though strains can be as large as 12 % (finite deformation stress and strain measures are used but the stress and strain are linearly related). Chapter 5 presents a study of effect of humidity on the evolution of a native oxide layer on a Si surface using angle resolved x-ray photoelectron spectroscopy (ARXPS). Chapter 6 investigates the mechanisms by which oxidation affects strength in silicon nanostructures. Chapter 7 extends the previous study of maintaining strength with a methyl monolayer [13] to longer time scales and a variety of organic surface coatings. Finally, Appendices A and B and C detail finite element mesh development and convergence, list the parameters used for the density functional theory (DFT) calculations presented in Chapter 4 and the molecular dynamics (MD) simulations presented in Chapter 6.

CHAPTER 2

METHODS

2.1 Fabrication of Si nanobeam specimens

The strength data presented in Chapters 6 and 7 were measured using nanoscale, single crystal Si double clamped beam specimens. A representative specimen is shown in Figure 2.1. The beams are nominally 12 µm long with a 5 µm long gauge section, 500 nm wide in the gauge section, and 100 nm to 200 nm thick. The beams were fabricated using a top-down process from a (1 1 1) oriented Si wafer specifically chosen to have very low miscut. The low miscut is important because the large aspect ratio; even a moderate miscut along the beam axis could result in significant thickness variation from one end to the other. The beam shown in Figure 2.1 is after strength testing and the notch is not a design feature but the characteristic failure mode.

The process to fabricate the beams is outlined schematically in Figure 2.2. The shape and thickness of the beams were defined with photolithography and reactive ion etching (Step a). Then a 100 nm annealed thermal oxide was grown (step b) which acted to protect the beam from wet chemical etching in a later step. A second round of of photolithography was performed and deep reactive ion etching defined the trench across which the beam would later span (step c).

The wafer was at this point diced into chips each containing a number of individual beams. Before proceeding, a chip was cleaned with a RCA cleaning procedure [14]. Wet chemical etching was then used to undercut the beams (step d). The chemical etchant attacks the crystalline Si only, allowing the SiO_2 to protect

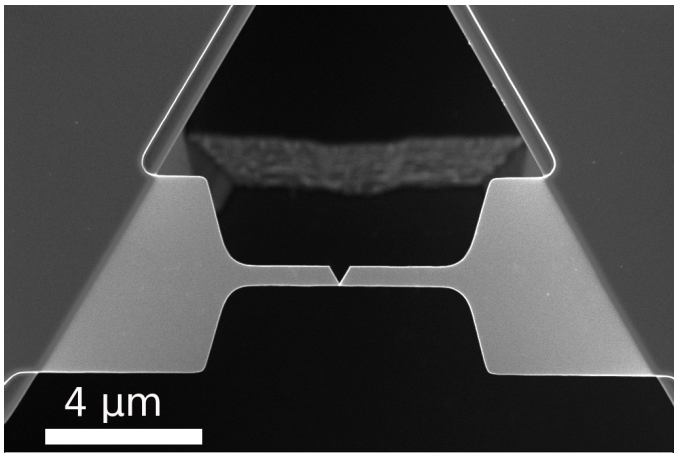

Figure 2.1: A nanoscale strength test specimen representative of those used to measure the data presented here

the top and sides of the beam from etching. Additionally, the chemical etches the Si anisotropically, effectively terminating on (1 1 1) planes. Since the bottom of the beam is (1 1 1) oriented, the etch terminates there and leaves the beam suspended across the trench. Two different chemical etchants were used for this step. Potassium hydroxide (KOH) was used for the majority of the undercutting process as it etches quickly but leaves a rough surface. Tetramethyl ammonium hydroxide (TMAH) was used as a finishing etch, resulting in an atomically smooth (1 1 1) surface. The chip was etched in KOH for 1 minute and 40 seconds and TMAH for 2 minutes and 40 seconds. Both etches were done at 72 °C.

In the final step (e), the oxide was removed with a buffered HF solution (5:1 HF:NH_4F) for 2 minutes, leaving the surface hydrogen terminated. In some cases, additional steps were performed to coat the surface with methyl groups or longer chain monomers. See Chapter 7 for more information on the surface coating process.

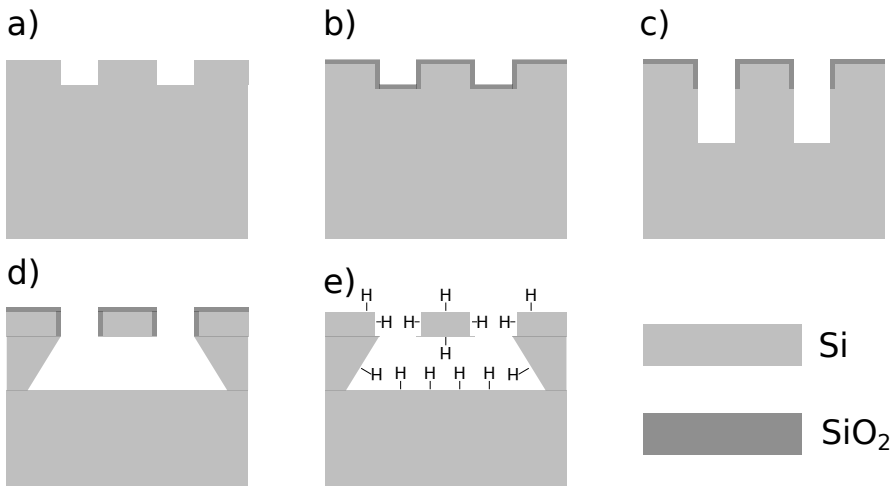

Figure 2.2: Schematic of the fabrication process for the Si nanobeam test specimens

2.2 AFM based fracture testing

The strength of the beams was tested using an atomic force microscope (AFM). A schematic of this process is shown in Figure 2.3. In an AFM, a cantilever with a sharp tip is placed over the surface. A laser is reflected off the back side of the cantilever onto a position sensitive photodetector (PSD). As the cantilever bends up or down, the laser will hit more of the top or bottom of the PSD. The PSD signal is sent to a feedback loop to control the height of the cantilever base to keep it at a constant deflection. It is then possible to scan the cantilever across the surface and create a map of the sample topography. This method is used to locate the geometric center of the beam.

Once the center of the beam is located, the cantilever is placed there and is made to push down on the beam. Both the cantilever and the beam will deflect, acting as springs in series. The deflection of the beam can be obtained by $\delta_{\text{beam}} = \delta_{\text{peizo}} - \delta_{\text{cant}}$ where δ_{beam} is the beam deflection, δ_{cant} is the cantilever deflection, and δ_{piezo} is the displacement applied by the piezo and the cantilever base. If the stiffness, k_{cant}, of the cantilever is known, the force applied to the beam can be obtained from

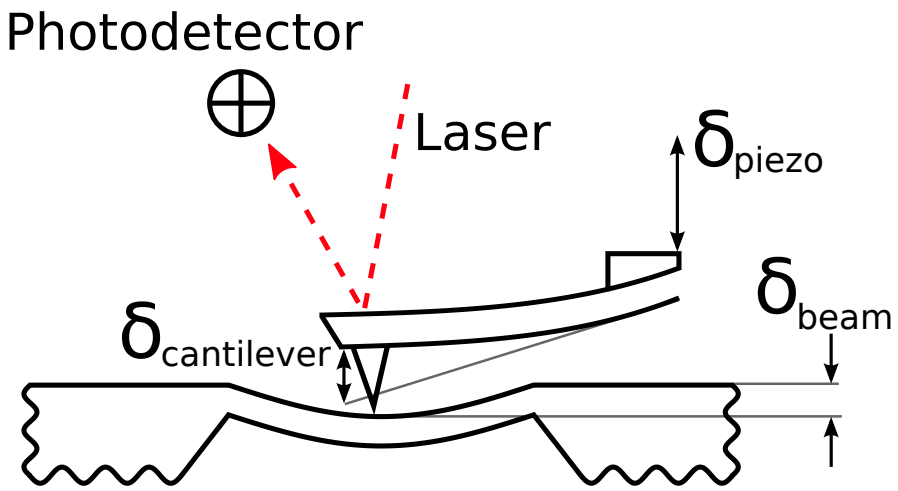

Figure 2.3: Schematic of the AFM based fracture testing process

$f_{\text{cant}} = k_{\text{cant}}\delta_{\text{cant}}$. A comparison of methods for measuring k_{cant} is presented in Chapter 3.

Using this method, the force applied to the beam and its deflection are recorded from onset of loading until failure. A plot of the force and deflection is shown in Figure 2.4. It is immediately clear that the structure responds nonlinearly. The typical bending behavior contributes an initial linear stiffness that is quickly overcome by a nonlinear membrane response. The membrane effect is a result of the beam deforming enough that the entire structure is in a state of tension. An Asylum MFP3D AFM was used for all beam strength testing.

2.3 Finite element modeling of beam structure

A finite element model was used to calculate failure stress from the force applied to the beam. For the model, the material was assumed to be anisotropic with the nonlinear stress measure linearly related to the nonlinear strain. Chapter 4 outlines and estimates of the error resulting from making this assumption of material

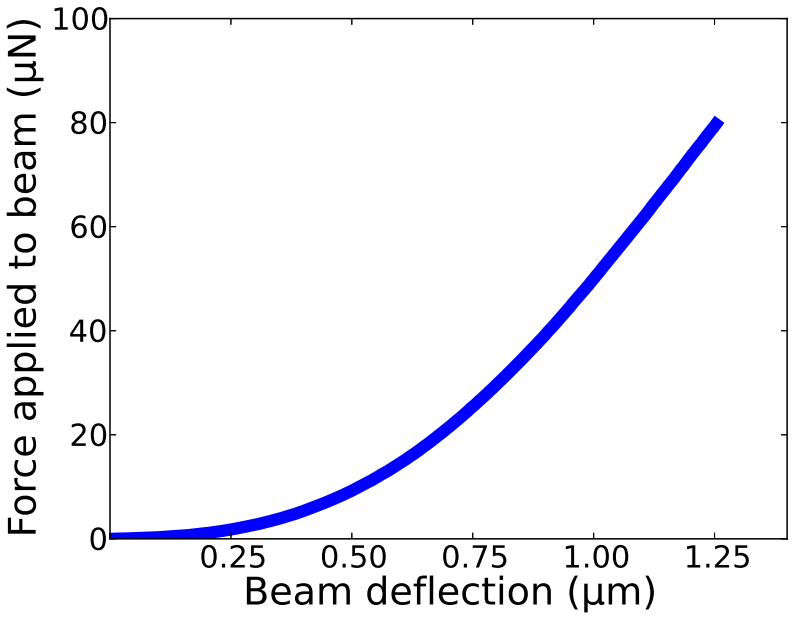

Figure 2.4: Force - deflection response of a beam sample showing its nonlinear structural behavior

linearity. The elastic modulii used were $C_{11} = 165.77\,\text{GPa}$, $C_{12} = 63.924\,\text{GPa}$, and $C_{44} = 79.619\,\text{GPa}$ [15], transformed to match the crystal orientation in the physical specimen. C3D10 10 node quadratic continuum tetrahedral elements were used with a high mesh density under the point of load application and transitioning to lower density elsewhere. A more detailed discussion of mesh development and convergence testing can be found in Appendix A. The model thickness was slightly changed to match the thickness calculated from the measured resonant frequency (described in Section 2.4) so that the resulting stress-force relation was accurate for that specific set of beams.

Bottom and side views of the model, deformed to a state close to where the physical samples failed, are shown in Figures 2.5a and 2.5b. Note in the bottom view that even though the structural response is dominated by the membrane effect there is still a large contribution to the stress from bending near the loading region.

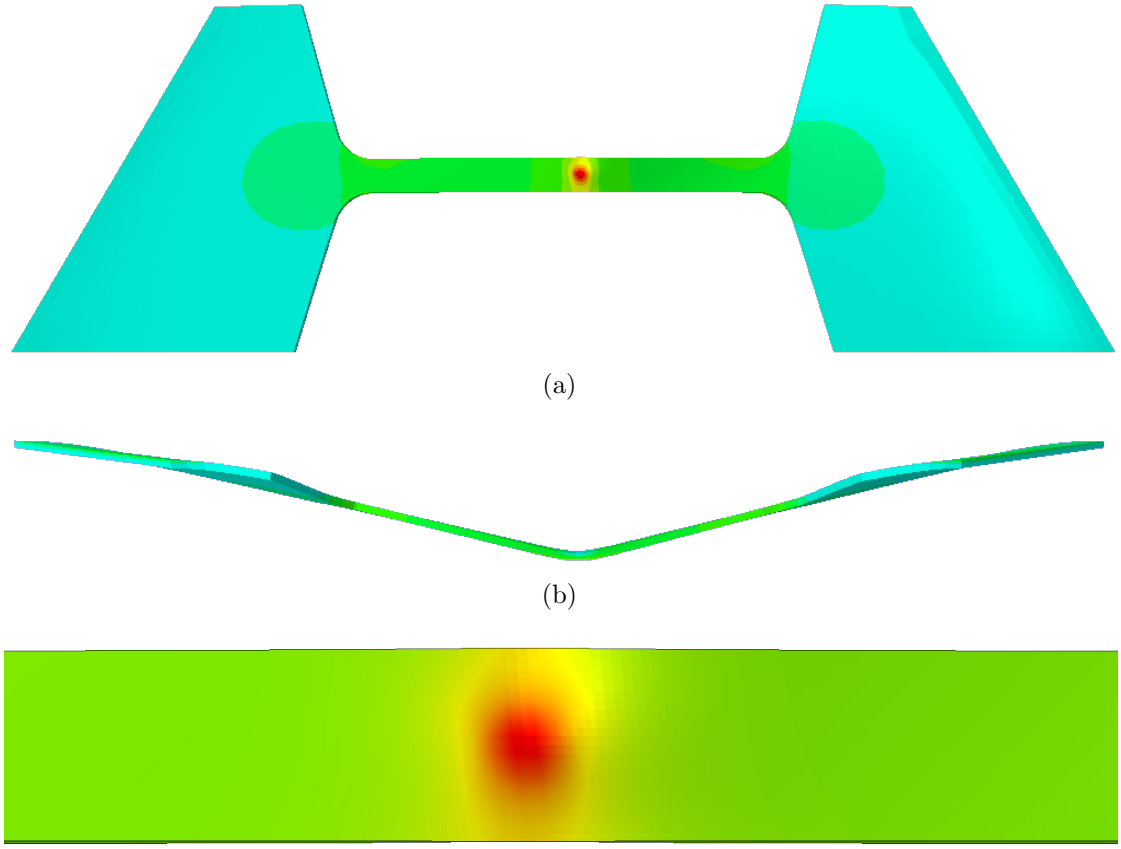

(a)

(b)

(c)

Figure 2.5: Bottom (a) and side (b) views of a finite element model of a beam specimen with (c) showing a closer view of the area of maximum stress, directly opposite the point of load application. Color indicates the normal component of stress along the long axis of the beam.

Figure 2.5c shows a closer view of the stress field on beam surface directly opposite the point of load application. This is the point of maximum stress and where failure initiates. In all three images, color indicates the normal stress in the direction along the long axis of the beam. Although Figure 2.5 shows the entire beam, due to symmetry only half was directly included in the FEA model. This is further discussed in Appendix A.

The evolution of the cross section of the beam at the center, at the point of load application, is shown in Figure 2.6. In all cases, color indicates the normal

component of strain in the transverse direction (horizontal in the figures). The scaling of the color is different in each step and is noted in the captions. In call cases, blue is most compressive strain, red is most tensile, with green and yellow depicting more moderate values. The deformed shape of the cross section is scaled 1:1.

In Figure 2.6a, the beam is unloaded and is stress and strain free. In Figure 2.6b, load is just starting to be applied. At this point the deformation is still in the linear bending regime. The gradient in the strain shows the anticlastic curvature associated with uniform bending plus some effects near load application. The beam is being bent up in this case, so the top is in compression along the long axis. The Poisson effect gives positive strain in the transverse direction at the top of the beam and negative strain along the bottom.

Figure 2.6c is about halfway to maximum load and the nonlinear membrane response is starting to take hold. Since the area of load application is small relative to the width of the beam the beam acts more like a plate in this region. For moderate to high forces, bending develops in the transverse direction as well as the long direction of the beam. As a result, an area of tensile strain is beginning to develop directly opposite load application. Anticlastic curvature is still seen near the edges of the beam, further from load application.

Figure 2.6d shows the fully loaded case at a state of deformation similar to that at experimental failure. Although anticlastic curvature is still seen at the edges, the area of tensile strain opposite the load application now dominates the overall cross section deformation.

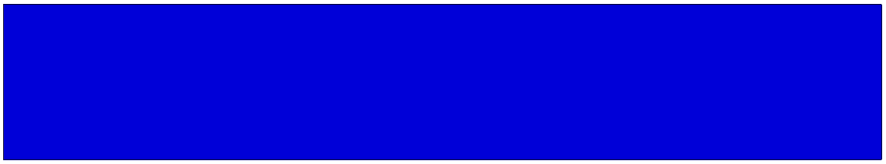

(a) Unloaded, strain zero everywhere

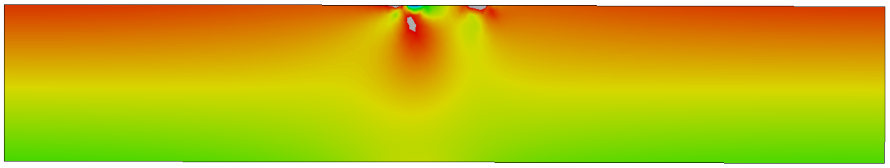

(b) Linear bending, color indicates strain ranging from -2×10^{-3} to 5×10^{-4}

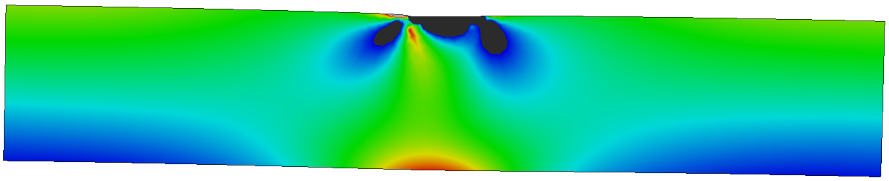

(c) Nonlinear regime, color indicates strain ranging from -5×10^{-3} to 1×10^{-3}

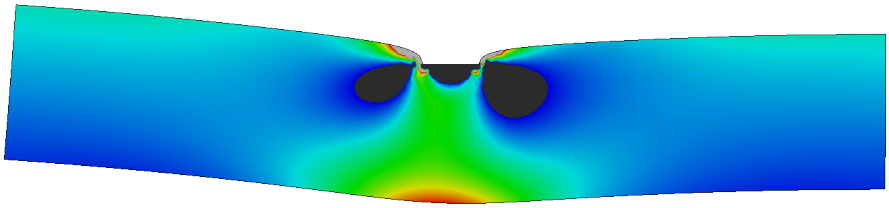

(d) Maximum loading, color indicates strain ranging from -0.02 to 0.06

Figure 2.6: Evolution of the cross section at beam center during load application. Color indicates normal strain in the transverse direction (horizontal in these figures) and the cross section deformation is scaled 1:1.

2.4 Resonant frequency based thickness measurement

While the exact shape of each beam specimen can be easily determined during the imaging phase of the AFM based fracture testing or using SEM, the thickness cannot be obtained the same way. Thickness is important to make an accurate finite element model to calculate stress from the force measured with AFM. The thickness was calculated by measuring the resonant frequency of each set of beams. The thickness of the finite element model was then adjusted until the resonant frequency calculated by the model matched the experimentally measured one. Resonant frequency was measured using the system depicted in Figure 2.7. The beams were mounted on a piezo and placed in a vacuum chamber which was pumped to about 1×10^{-5} mbar. A laser was sent through steering and focusing optics then through a linear polarizer. A polarized beam splitter then selected a single polarization to continue on to the microscope. Before the microscope, the laser went through a quarter wave plate which rotated the polarization 90°. The laser was focused through the microscope objective onto the beam surface, where it reflected and reversed its path back out of the microscope. After the polarization is rotated another 90° by the quarter wave plate, the beam has a polarization such that the beam splitter then sends the laser to an AC photodiode.

The piezo is swept through a frequency range which drives the oscillation of the beam structures. As the beams oscillate, they change the angle of reflection which affects the intensity measured at the photodiode. When the peizo driver is swept through the resonant frequency of the beam, the amplitude of oscillation peaks which results in a peak in the AC signal seen by the photodiode.

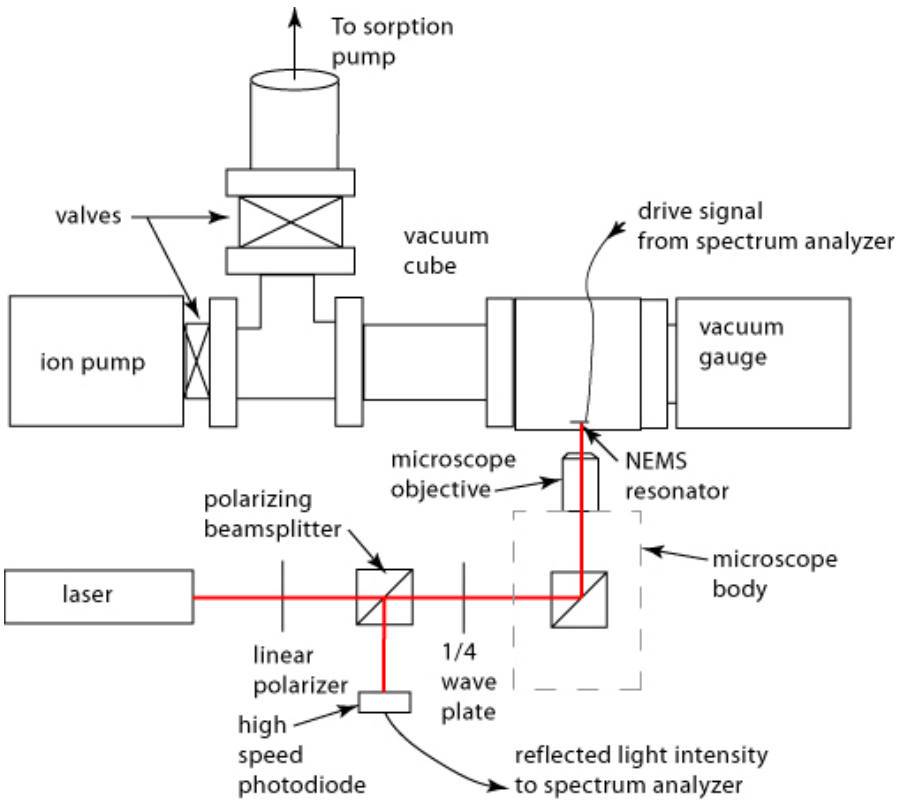

Figure 2.7: Schematic of the laser based system for measuring resonant frequency of the beam structures in order to calculated thickness

2.5 Statistical strength analysis

2.5.1 Weibull strength distributions

Since Si is a brittle material it fails in a stochastic manner. In order to sufficiently sample the strength distribution 10 to 15 beams are tested from each sample set. These strength values are then fit to a Weibull distribution. The Weibull distribution is predicated on a random distribution of flaws in a material and is commonly used for analysis of brittle materials. The Weibull distribution takes the form

$$P(\sigma) = 1 - \exp\left[-\left(\frac{\sigma}{\sigma_0}\right)^{\rho}\right] \tag{2.1}$$

where P is the cumulative probability of failure as a function of stress, σ, σ_0 is the Weibull stress and acts as an average value of the distribution, and ρ is the Weibull shape and controls the spread [16].

2.5.2 Maximum liklihood estimator

The experimental stress data are fit to the Weibull model with the maximum liklihood estimator (MLE) [17]. MLE uses a value called likelihood, L, which is the probability of the data set. Basic probability theory says that this should be the product of the probabilities of each data point,

$$L = L\left(\{\sigma_i\}; \sigma_0, \rho\right) = \prod_{i=1}^{N} p(\sigma_i; \sigma_0, \rho)\,. \tag{2.2}$$

Here, p is the probability density form of the Weibull distribution, obtained by taking the derivative of the cumulative probability form in Equation (2.1),

$$p(\sigma; \sigma_0, \rho) = \frac{dP(\sigma; \sigma_0, \rho)}{d\sigma} = \exp\left[-\left(\frac{\sigma}{\sigma_0}\right)^{\rho}\right]\left(\frac{\rho}{\sigma_0}\right)\left(\frac{\sigma}{\sigma_0}\right)^{\rho-1}. \tag{2.3}$$

Given a set of Weibull parameters, L is then the probability of obtaining this particular distribution. Equivalently, this can be turned around to state L as a function of the Weibull parameters given fixed strength data,

$$L = \tilde{L}\left(\sigma_0, \rho; \{\sigma_i\}\right) = \prod_{i=1}^{N} p(\sigma_i; \sigma_0, \rho)\,. \tag{2.4}$$

The Weibull parameters that best fit the data are those which have the highest probability of producing said data. In other words, the best fit Weibull parameters are those that maximize L. An optimization routine is done over the space of Weibull parameters to maximize L. For computational simplicity, the optimization is typically done over the logarithm of L so the product in Equation (2.4) becomes a sum,

$$\ln L = \ln \tilde{L}\left(\sigma_0, \rho; \{\sigma_i\}\right) = \sum_{i=1}^{N} \ln\left[p(\sigma_i; \sigma_0, \rho)\right]\,. \tag{2.5}$$

2.5.3 Uncertainty of Weibull strength

Uncertainty in the failure stress of a single beam specimen comes from thee main sources, cantilever stiffness k, a value called sensitivity, S, which relates the AFM PSD signal to cantilever deflection (discussed more in Section 3.2.4), and the positioning of the AFM cantilever tip at the center of the beam (this error in stress is denoted by $\delta\sigma_{\text{pos}}$). The force applied by the AFM cantilever to the beam is linearly related to k and S, so by propagation of variance [18],

$$\left(\frac{\delta f}{f}\right)^2 = \left(\frac{\delta k}{k}\right)^2 + \left(\frac{\delta S}{S}\right)^2\,. \tag{2.6}$$

This carries forward to uncertainty in stress by

$$\left(\frac{\delta\sigma}{\sigma}\right)^2 = \left(\frac{f}{F(f)}\frac{\partial F(f)}{\partial f}\frac{\delta f}{f}\right)^2 + \left(\frac{\delta\sigma_{\text{pos}}}{\sigma}\right)^2\,, \tag{2.7}$$

where $\sigma = F(f)$ is the finite element calculated stress as a function of force.

Propagating the uncertainty through the MLE to the Weibull strength is more complicated. First we use MLE to calculate the nominal Weibull parameters of the set of strength data. We then generate a large number of random Weibull data sets of the same size as the original data set with these nominal Weibull parameters and calculate the parameters of each random set. By looking at the spread of randomized Weibull parameters, we can get a confidence interval for our nominal parameters. Figure 2.8 shows the uncertainty in Weibull strength, σ_0, as a function of uncertainty in each strength data point for sample sizes of 15. The important thing to note is that even with perfect knowledge of each individual strength data point, a significant uncertainty in Weibull strength still exists. This is simply the result of sampling the infinite strength distribution with a finite number of points. Figure 2.9 shows uncertainty in Weibull strength decreasing with increasing sample size assuming no uncertainty in each strength point. Both Figures 2.8 and 2.9 assume a Weibull shape of $\rho = 10$. Error bars in later chapters use 10^4 randomly Weibull sets and confidence limits of 95 %.

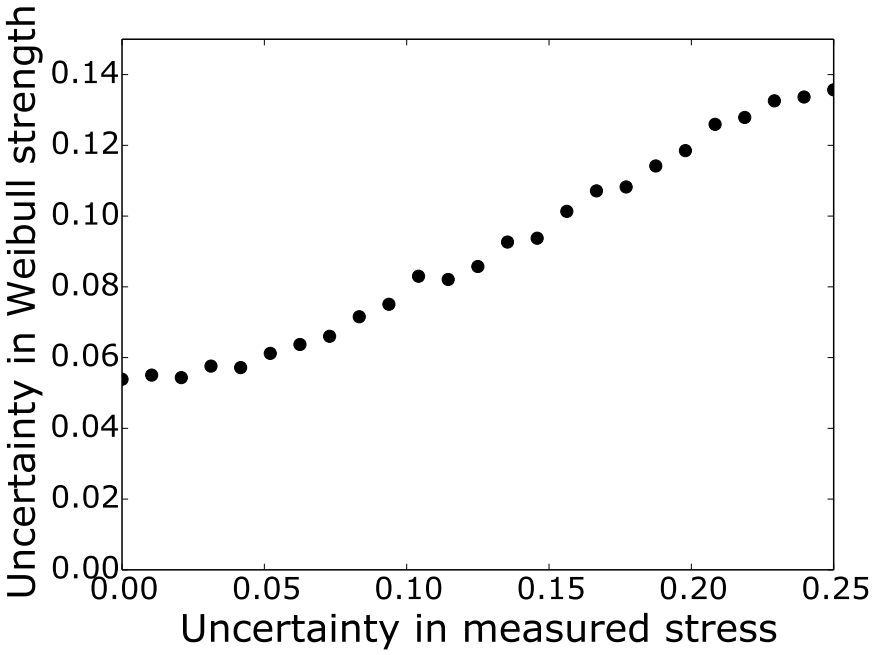

Figure 2.8: Uncertainty in Weibull strength as a function of uncertainty in each strength point for sample size of 15 and $\rho = 10$

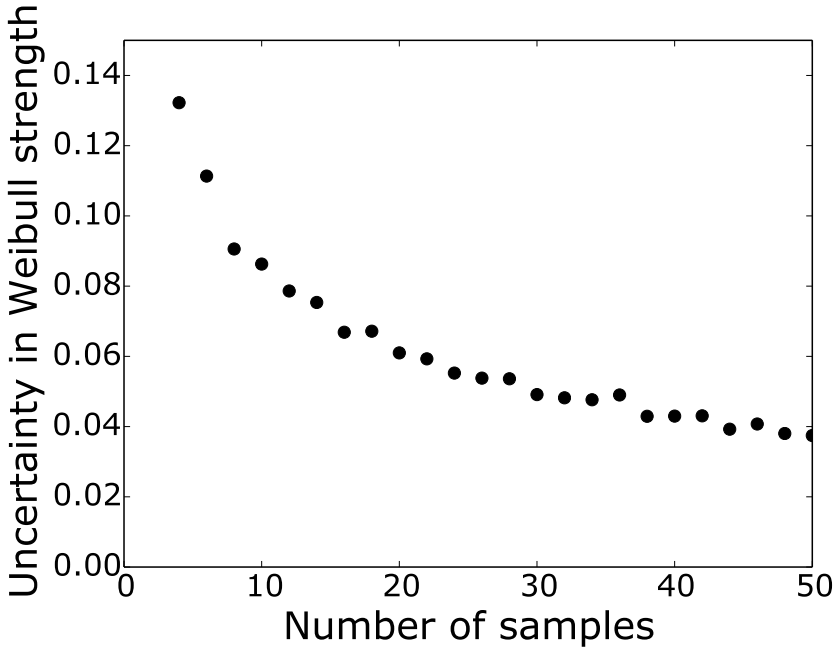

Figure 2.9: Uncertainty in Weibull strength as a function of sample size assuming no uncertainty in each strength point with $\rho = 10$

CHAPTER 3

AFM CANTILEVER CALIBRATION

3.1 Existing calibration methods and why they don't work

Atomic force microscopy (AFM), a variant of scanning probe microscopy, is a dominant instrument for mechanical properties measurements at the nano- and micro-scales. Measurements of mechanical properties, especially force-displacement responses, using AFM have been performed on systems ranging from the extremely compliant, such as molecular layers and cell membranes [19, 20], using very small forces (pN to nN), to the very stiff, such as silicon (Si) components of microelectromechanical systems (MEMS) devices [21], using much larger forces (up to 100s of µN).

The central element of most AFM instruments is a cantilever that deforms in response to contact with, or proximity to, the surface of the material or system being measured. In particular, the deflection or change in orientation of the free end of the cantilever is detected using diode-based position sensitive detectors (PSDs) that record the motion of a laser spot reflected from the back of the cantilever as the deflection changes. As the length/thickness ratio of the cantilever is usually very large, the displacement of the free end of the cantilever, Δz, is linearly related to the deflection. The change in force, Δf, exerted by the cantilever on the surface is related to the displacement, Δz, by the cantilever stiffness, $k = df/dz$. Hence, once a relationship between PSD output voltage and Δz of an AFM is established, Δf can be determined if k is known or calibrated.

3.1.1 Low stiffness methods

Compliant cantilevers are used for mechanical properties measurements such as molecular adhesion, as the displacement, and hence deflection, of the cantilever is large enough to generate measurable spot motion on the PSD under the influence of the very small forces involved. There are many methods available for calibrating the stiffness of such cantilevers, which typically have k values in the range 0.01 N/m to 1 N/m [22]. Many of these methods are based on measuring vibrational or resonance characteristics of the cantilever and using these characteristics to determine cantilever stiffness through mechanical or thermodynamic relations [23]. The large vibrational amplitudes and small resonant frequencies of compliant cantilevers enable the instrumentation within most commercial AFMs to implement these methods, often in an automated manner, and they suffice for most AFM applications [22].

Stiff cantilevers are required for mechanical properties measurements involving bulk material deformation, such as the fracture of nanoscale Si beams [12, 13], as the forces required are quite large by AFM standards. Because of high frequencies and small amplitudes, vibrational methods are poorly suited to calibrating the stiffness of such cantilevers, which, in the case of the nanoscale beam fracture measurements, had k values in the range 200 N/m to 250 N/m [24]. In order to apply AFM-based methods in quantitative assessments of the effects of different microfabrication techniques and surface treatments on fracture properties of nanoscale components, and mechanical properties of MEMS components more broadly, methods are required that are well-suited to the calibration of very stiff cantilevers. Such methods should specify the calibration accuracy (how closely the mean calibrated value estimates the true value) and precision (how closely repeated measurements

distribute about the mean value) [18].

3.1.2 Dimensional method

The stiffness of the test cantilever can be estimated based on the cantilever dimensions, geometry and the elastic properties of Si. Figure 3.1 shows a schematic diagram of the test cantilever. The length dimension L, the short and long lateral dimensions a and b, and the thickness t may all be measured using SEM or some other method. The finite element method is used for the stiffness computation and an analytical approximation is used as the basis for the uncertainty analysis.

To analyze the uncertainty, a beam theory based analytical approximation for the stiffness of the cantilever is used:

$$k = \frac{E_{\{110\}[110]} t^3 \left(a^2 + 4ab + b^2\right)}{12L^3 \left(a + b\right)} \tag{3.1}$$

where $E_{\{110\}[110]}$ is the Young's modulus of Si in the [110] direction (along the axial direction of the cantilever) with the $\{110\}$ plane (in this case the top or bottom surface of the cantilever) in a state of plane strain perpendicular to the (001) a and b faces and is given by [25]

$$E_{\{110\}[110]} = C_{44} + \frac{(C_{11} + 2C_{12}) \cdot (C_{11} - C_{12})}{2C_{11}} \tag{3.2}$$

with $C_{11} = 165.77$ GPa, $C_{12} = 63.924$ GPa, and $C_{44} = 79.619\,\text{GPa}$ [15]. The orientation of the cantilever was confirmed using Laué X-ray back reflection. The SEM measured values for L, a, b, and t were 112 µm, 24.7 µm, 54.6 µm, and 6.12 µm with repeatabilities of 0.81 %, 2.4 %, 0.74 %, and 4.6 %.

The relative uncertainty in k using this method can be calculated by applying

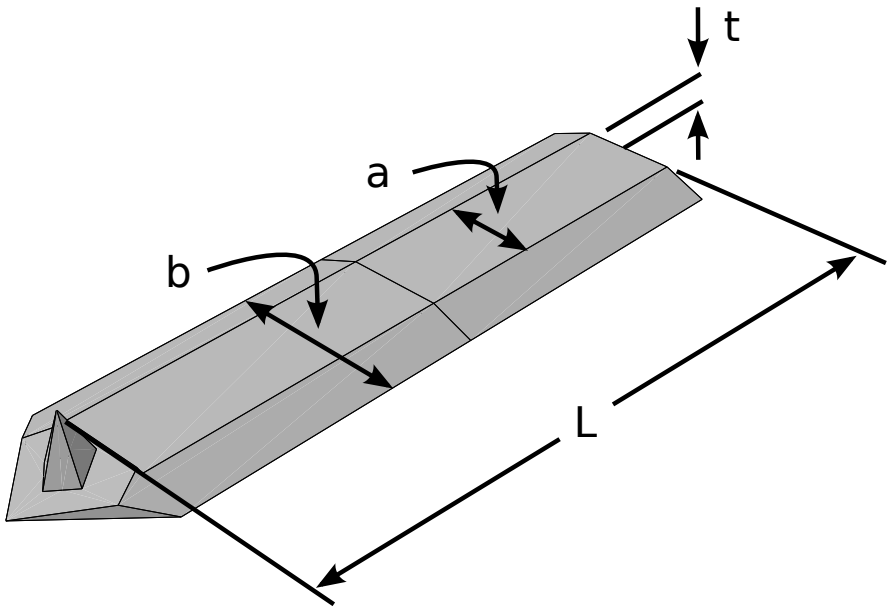

Figure 3.1: Schematic diagram of test cantilever, showing dimensions

propagation of variance [26] to Equation (3.1) resulting in

$$\left(\frac{\delta k}{k}\right)^2 = \left(3\frac{\delta t}{t}\right)^2 + \left(3\frac{\delta L}{L}\right)^2 + \left(\frac{a^3+2a^2b+3ab^2}{a^3+5a^2b+5ab^2+b^3}\right)^2\left(\frac{\delta a}{a}\right)^2 + \left(\frac{3a^2b+2ab^2+b^3}{a^3+5a^2b+5ab^2+b^3}\right)^2\left(\frac{\delta b}{b}\right)^2 + \left(\frac{\delta E_{\{110\}[110]}}{E_{\{110\}[110]}}\right)^2. \quad (3.3)$$

Substituting in the measured values and repeatabilities for L, a, b, t, and $E_{\{110\}[110]}$, using McSkimin's values for uncertainty in elastic modulii of Si [15], the maximum uncertainty is estimated to be 13.9 %. This value is almost entirely controlled by uncertainty in t, which when multiplied by its weighting factor of 3 contributes 13.6 % to the 13.9 % total uncertainty in k.

Stiffness is computed using finite element analysis which allows incorporation of effects such as the asymmetry of the cantilever base (see Figure 3.5). The FEM model used the measured cantilever dimensions and elastic moduli and gave a stiffness of $k = 231\,\mathrm{N/m}$. Taking into account the uncertainty analysis results in a stiffness of $k = 231 \pm 32$ N/m.

3.1.3 Resonant frequency method

In experiments where stiff cantilevers were used to measure the fracture strength of Si nanobeams [12, 13], cantilever stiffness was measured using a hybrid dimensional-resonant frequency method. In this case, only a top view SEM image, such as Figure 3.5a was available. While the L, a, and b may be measured using Figure 3.5a, the thickness dimension t is left unknown. In addition to measuring L, a, and b, the resonant frequency ω_0 was also measured in this method. The thickness of a finite element model was tuned so that the resonant frequency of the model matched the measured frequency. Once the frequencies were matched, the stiffness was calculated using the finite element model. Using this method results in a stiffness of $k = 183\,\mathrm{N/m}$.

The uncertainty in this method depends on uncertainty in the measured dimension L, a, and b as well as the uncertainty in Young's modulus $E_{\{110\}[110]}$ and resonant frequency. The relative uncertainty in density of Si is $1.1 \cdot 10^{-7}$ [27] and considered negligible in this analysis. A final source of error is the mass of the cantilever tip, m_{tip}. Because only a top view SEM image is used for dimensional measurements the length of the tip cannot be determined and the manufacturer nominal values must be used. This results in a large uncertainty in m_{tip} of $44.8\,\%$. Treating the tip as a point mass at the end of the cantilever, resonant frequency may be expressed as

$$\omega_0^2 = \frac{k}{m_{\mathrm{tip}} + CM} \tag{3.4}$$

where M is the mass of the body of the cantilever and $C = 0.23$ is a scaling factor allowing the distributed mass of the cantilever to be expressed as a point oscillator [28]. M may be expressed in terms of cantilever dimensions and the

density of Si, ρ,

$$M = \rho L t (a+b)/2\,. \tag{3.5}$$

Combining Equations (3.4) and (3.5) with Equation (3.1) relates cantilever thickness to measured parameters;

$$\omega_0^2 = \frac{E t^3 \left(a^2 + 4ab + b^2\right)}{12 L^3 (a+b)} \frac{1}{m_{\text{tip}} + 1/2 C \rho L t (a+b)}\,. \tag{3.6}$$

A computer algebra system was used to exactly solve Equation (3.6) for t, giving t as a function of measured parameters, $t = t(E_{\{110\}[110]}, a, b, L, m_{\text{tip}}, \omega_0)$. Uncertainty in t can then be found using propagation of variance analysis [26] (due to their complexity, the explicit forms of the partial derivatives are omitted here).

$$\begin{aligned}
\left(\frac{\delta t}{t}\right)^2 &= \left(\frac{E_{\{110\}[110]}}{t}\frac{\partial t}{\partial E_{\{110\}[110]}}\frac{\delta E_{\{110\}[110]}}{E_{\{110\}[110]}}\right)^2 + \left(\frac{a}{t}\frac{\partial t}{\partial a}\frac{\delta a}{a}\right)^2 + \left(\frac{b}{t}\frac{\partial t}{\partial b}\frac{\delta b}{b}\right)^2 + \\
&\qquad \left(\frac{L}{t}\frac{\partial t}{\partial L}\frac{\delta L}{L}\right)^2 + \left(\frac{m_{\text{tip}}}{t}\frac{\partial t}{\partial m_{\text{tip}}}\frac{\delta m_{\text{tip}}}{m_{\text{tip}}}\right)^2 + \left(\frac{\omega_0}{t}\frac{\partial t}{\partial \omega_0}\frac{\delta \omega_0}{\omega_0}\right)^2 \\
&= \left(-0.333\,\frac{\delta E_{\{110\}[110]}}{E_{\{110\}[110]}}\right)^2 + \left(-0.142\,\frac{\delta a}{a}\right)^2 + \left(-0.192\,\frac{\delta b}{b}\right)^2 + \\
&\qquad \left(1.000\,\frac{\delta L}{L}\right)^2 + \left(0.333\,\frac{\delta m_{\text{tip}}}{m_{\text{tip}}}\right)^2 + \left(0.667\,\frac{\delta \omega_0}{\omega_0}\right)^2 \\
&= 14.9\,\%
\end{aligned} \tag{3.7}$$

In this case, uncertainty is dominated by m_{tip}. All other terms contribute less than 1 % uncertainty when multiplied by their weighting factor. Using Equation (3.1), uncertainty in stiffness is $\delta k/k = 3\delta t/t = 45\,\%$ or a stiffness value of $k = 183 \pm 82$ N/m.

3.2 Reference cantilever method

In order to provide a lower uncertainty when measuring high stiffness values, a reference cantilever method was developed [29]. The use of a reference cantilever of known stiffness for calibration of the stiffness of a test cantilever for performing AFM measurements of small-scale mechanical properties is a multi-step process: (1) Load cell calibration[30]; (2) Instrumented indenter calibration[30]; (3) Reference Cantilever calibration [31–33]; and (4) Test cantilever calibration [30, 33–38]. The steps used here, along with the introduced uncertainties, are described below in turn.

3.2.1 Load cell calibration

A capacitance-based load cell described by Pratt, *et al.* [30] was calibrated using deadweight masses and an Andeen-Hagerling (Cleveland, OH) AH 2500A capacitance bridge. The masses, m, were NIST-certified (traceable back to a realization of a base unit of the SI system, in this case the kilogram) and ranged from nominally 0.5 mg to 500 mg and the applied force, $F = mg$, exerted by a mass on the load cell was calculated using a locally measured SI-traceable value of gravitational acceleration, g. The greatest uncertainty in the applied force was for the smallest mass (exerting nominally 5 µN force) and was ±0.1 % (all uncertainties in this paper quoted as percentages are relative uncertainties: the uncertainty in a quantity divided by its mean or best estimated value). Application of a mass to the load cell resulted in a change in cell capacitance, ΔC; once again the greatest uncertainty in the capacitance change was for the smallest mass and was ±0.2 % (uncertainty in the capacitance output arose primarily from the resolution of the capacitance

bridge). The load cell was calibrated by fitting the force-capacitance change data to a cubic polynomial of the form $F = A_3(\Delta C)^3 + A_2(\Delta C)^2 + A_1(\Delta C)$; the greatest residual deviation between the fitted and measured forces was 0.2 %.

3.2.2 Instrumented indenter calibration

The load and displacement outputs of an instrumented indenter, Hysitron Triboindenter (Eden Prairie, MN), were calibrated using the calibrated capacitance load cell and an optical interferometer, respectively. A spherical probe was loaded onto the load cell. The indentation force recorded by both the indenter internal measurement system and the external calibrated cell were compared. The proportionality constant relating the forces from these two sources provided the calibration of the indenter force output. Repeated applications of nominal forces of 10 µN and 50 µN in the target testing range gave standard deviations in the calibrated indenter mean force output of 1.5 % and 0.7 % respectively; additional, small, uncertainty in the indenter force output arose from time variation in the output. Summing all uncertainties in quadrature, from both the capacitance and indenter force systems, resulted in a total indenter force calibration uncertainty (over the force range used) between 1 % and 2 %. Linearly interpolating between these values to a force of 25 µN provided a characteristic indenter force uncertainty of ±1.7 %. The displacement of the indenter was calibrated using an inferometer system designed by our collaborators in the Nanomechaical Properties Group at NIST [39]. The system, based on a 1550 nm fiber-optic laser source, used a Fabry-Perot cavity established between the end of the indenter shaft and the specimen mounting stage to measure the displacement of the shaft over a range of travel of 4 µm with an accuracy well below 1 nm. Displacement as determined by the inferometer was then compared to

the displacement reported by the indenter. Using this method, the uncertainty in the Triboindenter displacement was found to be ±0.3 %.

3.2.3 Reference cantilever calibration

The stiffness of the reference cantilever, AppNano (Santa Clara, CA), ACL-TL, was calibrated using the calibrated instrumented indenter. The reference cantilever, shown in the scanning electron microscope (SEM) image of Figure 3.2, was selected for four important characteristics: stiffness, length, tip, and shape. The stiffness was selected to be as close as possible to that of the test cantilevers so as to provide the spring constant matching that reduces uncertainties in the test cantilever calibration process [35, 36]. The ACL-TL has a nominal stiffness of 45 N/m, although the group of candidate reference cantilevers was hand selected to have greater than average stiffness of at least 60 N/m. A tipless, picket-shaped, long reference cantilever (Figure 3.2) was selected to reduce uncertainties in stiffness arising from uncertainty in the loading location of the cantilever. The lack of a tip and the picket end shape enabled repeatable placement of the indentation probe on the reference cantilever using the angular cues of the picket end and without having to avoid a tip. While it would be desirable to have a stiffer reference cantilever to increase spring constant matching, the placement repeatability afforded by the lack of a tip provides a greater reduction in overall uncertainty than the difference in stiffnesses. Repeatability of loading location was within 1 µm; this location is indicated by the white cross superimposed in Figure 3.2. As the stiffness of a cantilever varies in a cubic manner with distance of the loading location to the clamped, built-in end, long cantilevers reduce stiffness uncertainties arising from uncertainties in the loading location. The reference cantilever was approximately 220 µm long. As the

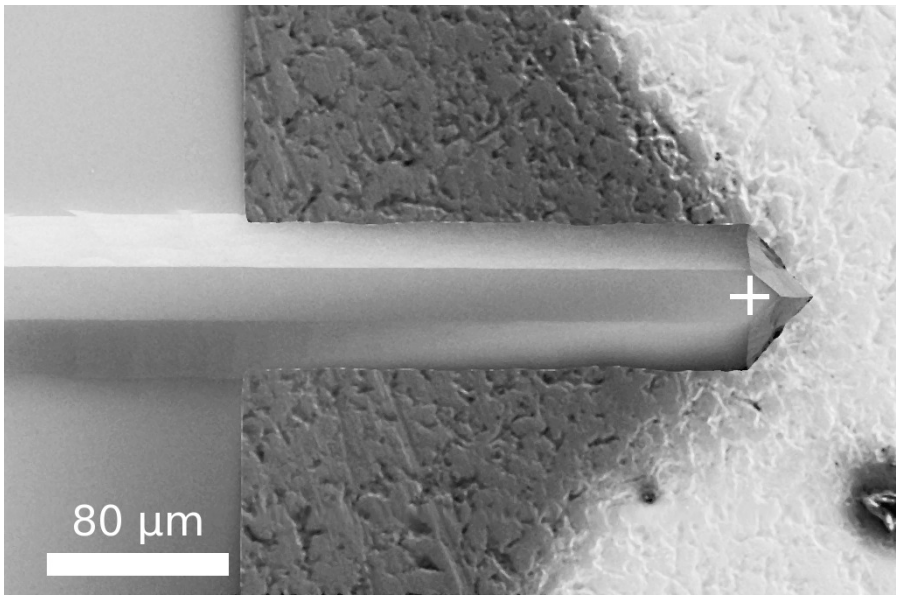

Figure 3.2: SEM micrograph of a reference cantilever

reference cantilever stiffness was calibrated at the exact location used for calibrating the test cantilever there was no need to account for length anomaly corrections [32, 33, 37].

A typical reference cantilever force-displacement calibration response obtained using the instrumented indenter is shown in Figure 3.3, and a schematic diagram of the calibration method is shown in Fig. 3.4(a). Both loading and unloading data are shown in Fig. 3.3 and the response displays little noise or hysteresis and excellent linearity. The slope of this line provides the reference cantilever calibrated stiffness and the standard error of the slope provides the stiffness uncertainty for that particular measurement. For the reference cantilever used for this study, the calibration was repeated 20 times (10 times on two different days) providing a calibrated stiffness value, k_{ref}, of 76.7 ± 0.6 N/m, where the uncertainty represents the statistical repeatability uncertainty of one standard deviation. Combining this uncertainty in quadrature with the instrumented indenter calibration uncertainty provides a total reference cantilever stiffness uncertainty of ± 1.9 %.

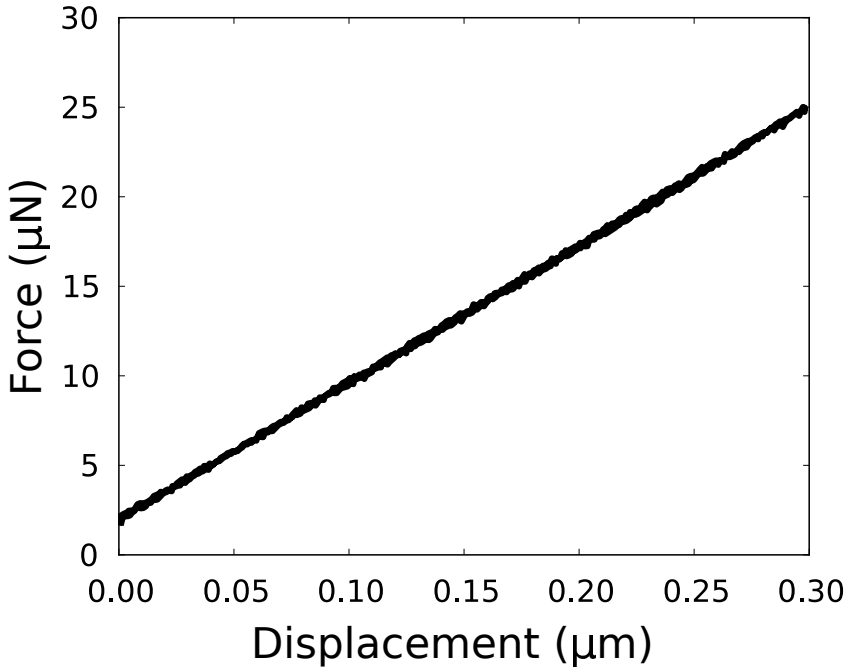

Figure 3.3: Single force-displacement response of a reference cantilever

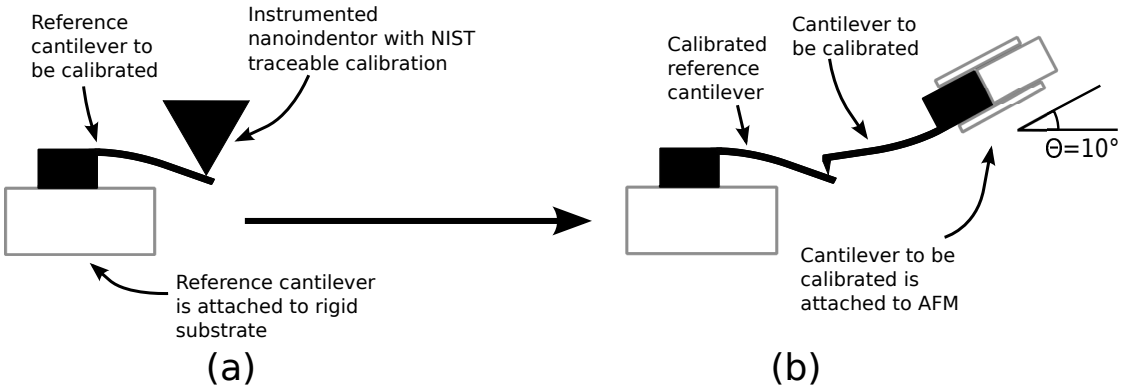

Figure 3.4: Schematic diagram of a reference cantilever deformed by indenter (a) and then test cantilever (b)

3.2.4 Test cantilever calibration

The stiffness of the test cantilever, an uncoated TAP525, Bruker AFM Probes (Camarillo, CA), MPP-13100-10 with a nominal stiffness of 200 N/m was calibrated using the previously calibrated reference cantilever and an AFM, Bruker Dimension 3100 (Santa Barbara, CA). Bottom- and side-view SEM images of the test cantilever are shown in Figure 3.5. The test cantilever calibration was a two-step process. In the first step, the reference cantilever was mounted on a stiff substrate on the AFM stage and the test cantilever was clamped in the piezoelectric scanning system of the AFM in the usual manner. The tip at the free end of the test cantilever was then placed over the bulk Si base of the reference cantilever and the clamped end of the test cantilever displaced in the vertical direction by the AFM piezoelectric drive. Contact of the test cantilever tip with the reference cantilever base led to deflection of the test cantilever and a change in the PSD output signal. If the reference cantilever base is approximated as rigid, the displacement of the free end of the test cantilever relative to the clamped end is equal to the imposed AFM piezoelectric displacement; the ratio of the imposed displacement to the PSD output voltage is then the optical lever sensitivity of the AFM, S_1. A representative plot of output voltage as a function of imposed piezoelectric displacement enabling the determination of S_1 is shown in Figure 3.6. Initially the PSD output voltage was invariant as the cantilever approached the base surface. As the tip approached the surface, the output decreased slightly reflecting van der Waals interactions between the tip and the surface and a small attractive tip-surface interaction. Once the tip was fully in contact with the surface the PSD output increased linearly as the cantilever deflected upward in a repulsive interaction. The inverse slope of this linear variation is S_1.

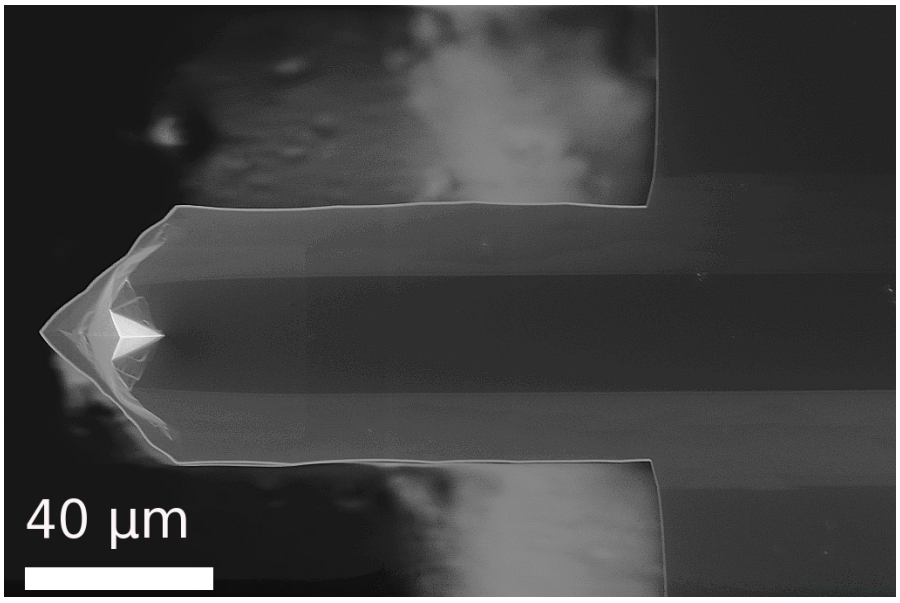

(a)

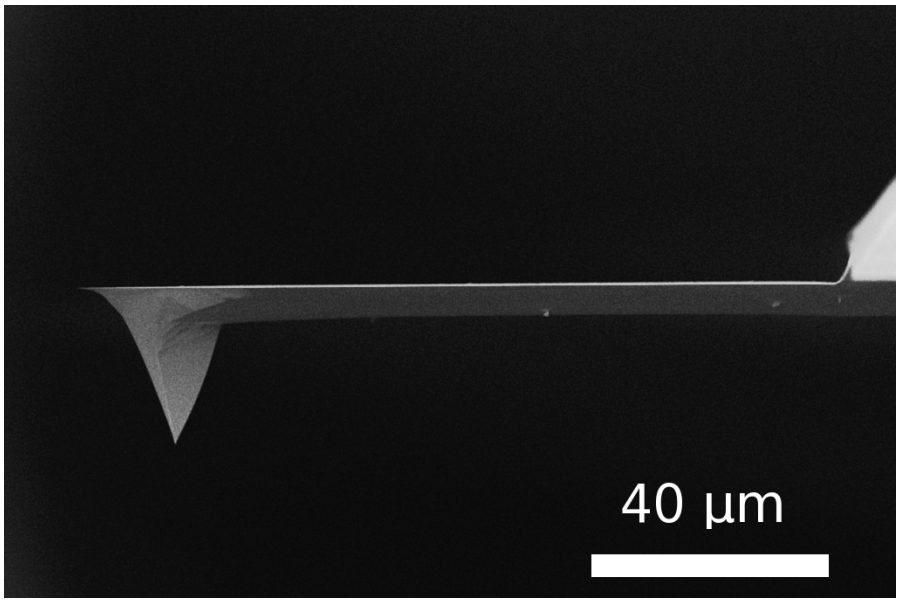

(b)

Figure 3.5: Top (a) and side (b) view SEM micrographs of a test cantilever

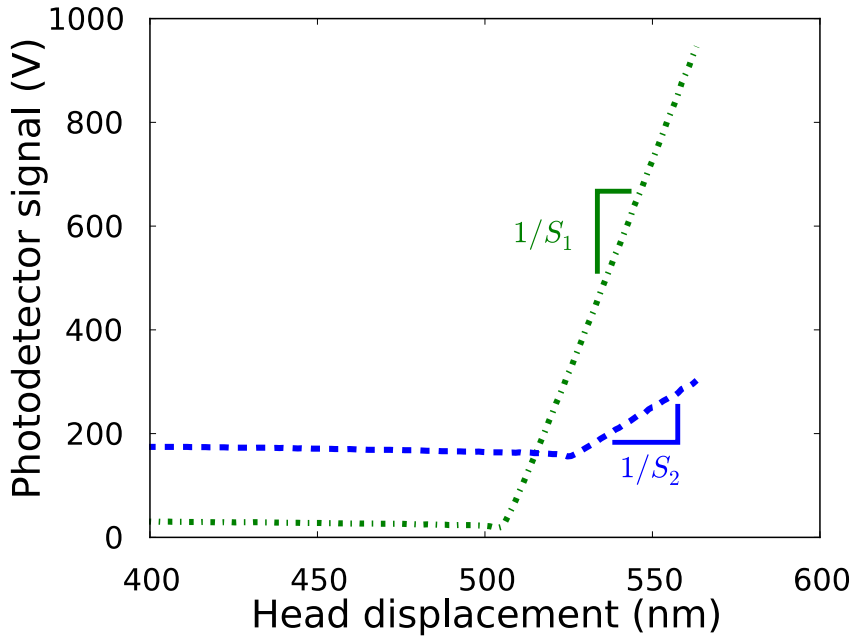

Figure 3.6: S_1 and S_2 measurement data with linear fits

In the second step, the tip of the test cantilever was aligned over the free, picket-end, location at which the reference cantilever was calibrated and a second PSD output-imposed displacement response was measured. The test cantilever pushed on the reference cantilever and both deflected, as shown in Fig. 3(b), acting as springs in series. Hence, the AFM head traveled through a greater distance to produce the same test cantilever deflection. As a consequence, the slope of the resulting linear region of the response in the second step was less than that in the first, as shown in Figure 3.6. The inverse of this second slope is S_2. The stiffness of the test cantilever, k, can be determined from S_2, S_1, and k_{ref}, after correcting for the orientation of the test cantilever. The test cantilever was mounted in the AFM head at an angle, θ, of 10° relative to the reference cantilever, as shown in Figure 3.4(b). The stiffness of the test cantilever is given by [37]

$$k = \left(\frac{S_2}{S_1} - 1\right) k_{\text{ref}} \cos^2(\theta) \ . \tag{3.8}$$

Ten measurements of the test cantilever response to determine S_1 and S_2 were

Table 3.1: Summary of stiffness values and uncertainties for the three methods discussed

Method	Stiffness (N/m)	Uncertainty
Reference cantilever	218 ± 16	7.4 %
Dimensional	231 ± 32	13.9 %
Hybrid dimensional-resonance	183 ± 82	45 %

taken over two days (five each day) which generated a repeatability uncertainty for k of 7.2 %. The mean values for S_1 and S_2 were 63.14 nm/V and 270.7 nm/V respectively. The test cantilever was remounted and laser spot adjusted before each measurement to make each measurement as independent as possible. Combining this value with the reference cantilever stiffness uncertainty (1.9 %) led to a total uncertainty of the test cantilever stiffness of ± 7.4 %, or, using the mean values of S_1 and S_2, $k = 218 \pm 16$ N/m.

3.3 Summary of stiffness values and uncertainty

The stiffness values and uncertainties of each method are summarized in Table 3.1. Note that in addition to being SI-traceable, the reference cantilever method has the smallest uncertainty of the three methods. Thus the reference cantilever method is of great benefit in experiments such as the AFM based stochastic fracture testing of nanostructures, discussed below, where accurate stiffness calibration is required to quantitatively measure strength and small uncertainty is needed to discern actual strength variations.

CHAPTER 4

CONSTITUTIVE MODELING

4.1 Constitutive assumptions

Throughout this work, we assume a Si constitutive model that is anisotropic with cubic symmetry and a linear relation between strain and stress. Later sections will show that strains as high as 12 % can be experienced during fracture testing of the Si beam specimens. While 12 % is not an exceptionally large strain for some materials, such as polymers, it is very uncommon for crystalline structures to withstand strains this high. *Ab inito* simulations of tension and shear mode deformations on a $\{1\,1\,1\}$ plane [40] show that a 12 % strain is high enough that the stress strain relationship is beginning to deviate from linear. In order make an estimate of the error produced by using an elastic constitutive model this chapter develops a simple hyperelastic model that can be applied to the deformation of the Si beams.

Since Si is a crystalline material with cubic symmetry, a true hyperlastic model would have to account for this anisotropy. In order to build an invariant based representation function of an anisotropic material, one typically looks for a strain energy function of the form

$$W = W(\mathbf{F};\, \mathbf{A}) \tag{4.1}$$

where W is an isotropic function of deformation gradient $\mathbf{F}$ and all of the anisotropic properties are contained in $\mathbf{A}$. $\mathbf{A}$ is typically called a structural tensor. Boehler [41] and Zheng [42] contributed major efforts in the development of structural tensors in producing constitutive relations that are isotropic in space for anisotropic materials. Due to the fact that crystalline materials rarely see such high strains, very little

work has been done to produce such a constitutive model for Si, the most complete being a MIT PhD thesis giving representation functions for diamond and Si as a function of eight strain invariants [43]. Since in our case the structural response is controlled entirely by the tensile response of the $\langle 1\,\bar{1}\,0\rangle$ direction we can approximate the system as isotropic with stiffness matching the $\langle 1\,\bar{1}\,0\rangle$ behavior.

4.2 Density Functional Theory

Rather than using experimental data to create our simplified hyperelastic constitutive model we have used density functional theory (DFT) to calculate the stress-strain response in a $[1\,\bar{1}\,0]$ direction from first principles. DFT is a numerical method of solving Schrödinger's Equation, the governing equation of quantum mechanics [44],

$$\widehat{H}\varphi = \left[\widehat{T} + \widehat{U} + \widehat{V}\right]\varphi = \left[\sum_i \frac{-\hbar^2}{2m_i}\nabla_i^2 + \sum_i U(\mathbf{r}_i) + \sum_{i<j} V(\mathbf{r}_i, \mathbf{r}_j)\right]\varphi = E\varphi\,. \tag{4.2}$$

$\widehat{T}$ is the kinetic energy operator, U is the externally applied potential, in this case the potential field of the positively charged nucleus, and V is the electronic interaction potential. While U is known *a priori*, V depends on the wavefunction and makes this a nonlinear problem. The kinetic and potential energy operators add to form the Hamiltonian operator, $\widehat{H}$.

In DFT, the nuclear positions are assumed to be known and Equation (4.2) is used to calculate electronic behavior only. The wavefunction, φ, carries all information about the state of the system. For example, electron density is given by $\rho(\mathbf{r}) = \varphi(\mathbf{r})\varphi(\mathbf{r})$ and the average value of some quantity A by

$$\langle A\rangle = \langle\varphi(\mathbf{r})|\,\widehat{A}\,|\varphi(\mathbf{r})\rangle = \int_\Omega \bar{\varphi}(\mathbf{r})\widehat{A}\varphi(\mathbf{r})d\Omega\,, \tag{4.3}$$

where $\widehat{A}$ is an operator corresponding to the quantity A and an overbar indicates complex conjugate.

It can be shown that there is a one-to-one correspondence between $\rho(\mathbf{r})$ and $\varphi(\mathbf{r})$ [45]. DFT takes advantage of this and calculates the real valued $\rho(\mathbf{r})$ rather than the complex valued $\varphi(\mathbf{r})$. To do this, operate from the left on Equation (4.2) with φ and divide by $\langle\varphi|\varphi\rangle$ to get

$$E = \frac{\langle\varphi|\,\widehat{H}\,|\varphi\rangle}{\langle\varphi|\varphi\rangle} = \langle\varphi|\,\widehat{T} + \widehat{U} + \widehat{V}\,|\varphi\rangle = \int_{\Omega} f\left[\mathbf{r}, \boldsymbol{\nabla}\mathbf{r}\right] d\Omega\,. \tag{4.4}$$

Equation (4.4) is exact for the $\widehat{U}$ and $\widehat{V}$ terms. Some approximation is required in the $\widehat{T}$ term to express the $\langle\varphi|\,\nabla^2\,|\varphi\langle$ in terms of $\rho(\mathbf{r})$. In this work, the local density approximation (LDA) was used, which assumes kinetic energy is a function of electron density only. Other methods, such as generalized gradient approximation (GGA) assume kinetic energy is a function of both electron density and its gradient.

Total system energy is now a functional of electron density, which is a function of position. The ground state of the system can be found by minimizing this energy functional. To do this numerically, $\rho(\mathbf{r})$ is expanded in a basis set, typically plane waves for periodic crystal systems.

4.3 DFT model definition

Si has a diamond cubic crystal structure. This means it is face-centered cubic with an extra atom located at (¼, ¼, ¼) from each FCC atom. Since we are interested in the tensile behavior in the $\langle 1\,\overline{1}\,0\rangle$ direction and want to allow for contraction in the orthogonal direction we look for a unit cell with lattice vectors in the $\langle 1\,\overline{1}\,0\rangle$, $\langle 1\,1\,0\rangle$, and $\langle 0\,0\,1\rangle$ directions. The simplest such unit cell has four atoms located at

(0, 0, 0), (½, 0, ¼), (½, ½, ½), and (0, ½, ¾) with the $\langle 0\,0\,1\rangle$ direction $\sqrt{2}$ times as long as the $\langle 1\,\bar{1}\,0\rangle$ and $\langle 1\,1\,0\rangle$ directions. This unit cell is shown in Figure 4.1. All DFT simulations presented here used a kinetic cutoff energy of 100 Ry, a k-grid of $10 \times 10 \times 8$ points, and a lattice size of 10.21 Bohr. The accepted experimental lattice size is 10.26 Bohr. For more details on these parameters see Appendix B.

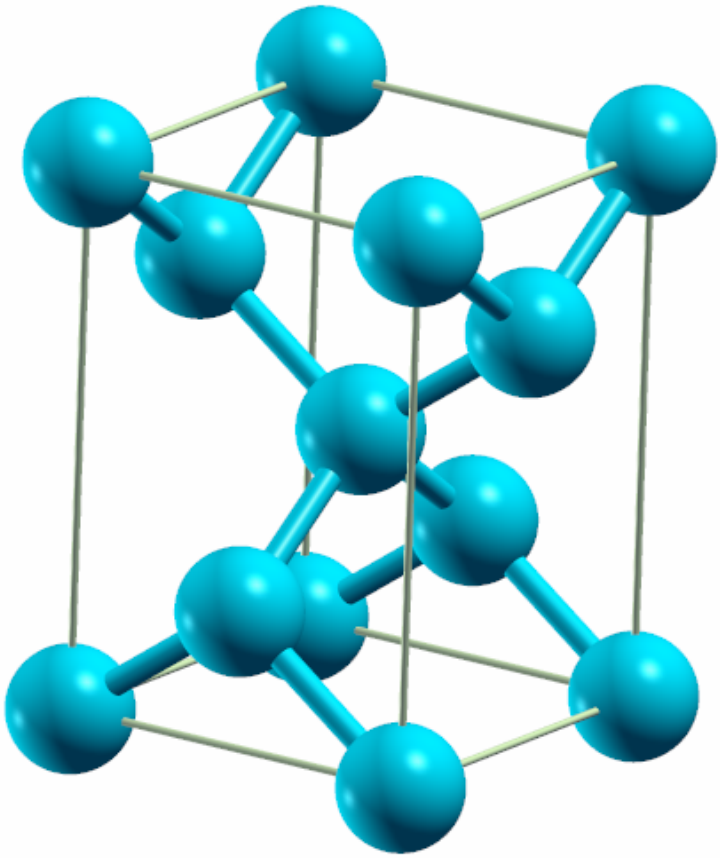

Figure 4.1: Four atom unit cell used in DFT calculations. Although 13 atoms are shown, only four are unique (the corner atoms are identical, for example).

In order to calculate the tensile stress-strain response, the $\langle 1\,\bar{1}\,0\rangle$ unit cell dimension is varied in a stepwise fashion starting from the relaxed state. At each strain state, the atomic positions are allowed to vary to minimize energy. In addition, the $\langle 1\,1\,0\rangle$ and $\langle 0\,0\,1\rangle$ lattice dimensions are relaxed. This allows for a Poisson contraction effect. The relaxed atomic positions from one strain state are

used as a starting point for the next strain state. In addition to the tensile response, the volumetric response was also calculated. In this, the unit cell was uniformly expanded at each strain state and only the atomic positions were allowed to relax.

4.4 DFT results

Figure 4.2 shows the total energy as function of Green strain, $\mathbf{E}$ in the $\langle 1\,\bar{1}\,0\rangle$ direction. Stress can be calculated using one of two methods. In the first, the energy shown in Figure 4.2 is assumed to be the strain energy $\Psi(\mathbf{E})$ and the second Piola-Kirchhoff (PK2) stress is then

$$\mathbf{P} = \frac{\partial \Psi}{\partial \mathbf{E}}\,. \tag{4.5}$$

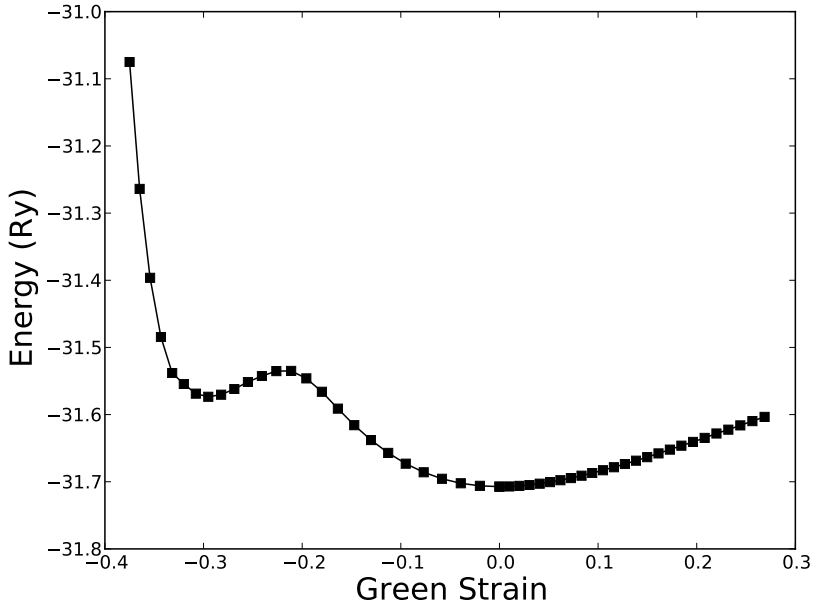

Figure 4.2: Total converged energy as a function of Green strain, $\mathbf{E}$

The second method of stress calculation is similar to the first except the energy derivative is performed quantum mechanically via the Helmann-Feynman

Theorem [45]. The Helmann-Feynman Theorem states that the derivative of the total system energy with respect to some parameter is the expectation value of the derivative of the Hamiltonian with respect that parameter. To see this, take the derivative of E with respect to a parameter λ and expand using chain rule,

$$\frac{\partial E}{\partial \lambda} = \frac{\partial}{\partial \lambda} \langle \varphi_\lambda | \, \widehat{H}_\lambda \, | \varphi_\lambda \rangle \tag{4.6}$$

$$= \left\langle \frac{\partial \varphi_\lambda}{\partial \lambda} \middle| \widehat{H}_\lambda \middle| \varphi_\lambda \right\rangle + \left\langle \varphi_\lambda \middle| \frac{\partial \widehat{H}_\lambda}{\partial \lambda} \middle| \varphi_\lambda \right\rangle + \left\langle \varphi_\lambda \middle| \widehat{H}_\lambda \middle| \frac{\partial \varphi_\lambda}{\partial \lambda} \right\rangle . \tag{4.7}$$

In the first term, $\widehat{H}_\lambda \, | \varphi_\lambda \rangle$ can be replaced by $E_\lambda \, | \varphi_\lambda \rangle$ following Equation (4.2) and since E_λ is a scaler it can be taken out of the inner product. A factor of E_λ can be taken out of the third term from $\langle \varphi_\lambda | \, \widehat{H}_\lambda$ in the same way. The right side of Equation (4.6) then becomes

$$E_\lambda \left\langle \frac{\partial \varphi_\lambda}{\partial \lambda} \middle| \varphi_\lambda \right\rangle + \left\langle \varphi_\lambda \middle| \frac{\partial \widehat{H}_\lambda}{\partial \lambda} \middle| \varphi_\lambda \right\rangle + E_\lambda \left\langle \varphi_\lambda \middle| \frac{\partial \varphi_\lambda}{\partial \lambda} \right\rangle . \tag{4.8}$$

The first and third terms can be combined into a single derivative of $\langle \varphi_\lambda | \varphi_\lambda \rangle$ to give

$$E_\lambda \frac{\partial}{\partial \lambda} \left\langle \varphi_\lambda \middle| \varphi_\lambda \right\rangle + \left\langle \varphi_\lambda \middle| \frac{\partial \widehat{H}_\lambda}{\partial \lambda} \middle| \varphi_\lambda \right\rangle . \tag{4.9}$$

Since $\langle \varphi_\lambda | \varphi_\lambda \rangle$ is simply the electron density integrated over the problem domain, this should always be normalized to unity and the derivative with respect to λ vanishes. Helmann-Feynman Theorem then states

$$\frac{\partial E}{\partial \lambda} = \left\langle \varphi_\lambda \middle| \frac{\partial \widehat{H}_\lambda}{\partial \lambda} \middle| \varphi_\lambda \right\rangle . \tag{4.10}$$

If λ is some strain measure $\boldsymbol{\epsilon}$, then Equation (4.10) calculates a stress measure $\boldsymbol{\sigma}$ that is work-conjugate to $\boldsymbol{\epsilon}$. Since the DFT calculation in each strain step is done independent of each other forces are in the deformed state. Energy density is calculated with respect to the original unit cell volume however. The stress measure calculated by Equation (4.10) must therefore be the Cauchy stress, $\mathbf{T}$. In order to

compare it to stresses calculated with the first method it must be converted to a PK2 stress using

$$\mathbf{P} = \det(\mathbf{F})\mathbf{F}^{-1}\mathbf{T}\mathbf{F}^{-\mathrm{T}}\,. \tag{4.11}$$

Figure 4.3 shows the PK2 stress as a function of Green strain calculated using both methods. As a comparison, Figure 4.4 shows the same quantities pulled forward to the deformed configuration (Cauchy stress as a function of Eulerain strain).

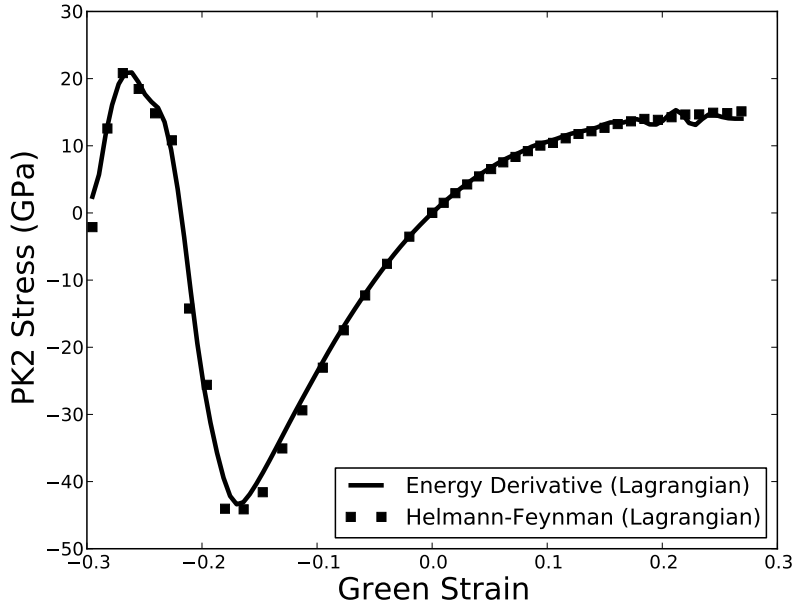

Figure 4.3: PK2 stress as a function of Green strain calculated using both methods described in the text

The tangent modulus of both Figure 4.3 and 4.4 around the relaxed state is 161 GPa, which is about 4.7 % different from the accepted value of 169 GPa. The response remains linear over quite a large strain range in the deformed configuration, which is typical of single crystal systems. As expected, the response stiffens in compression, paying an ever increasing price for further compressing the material, and becomes more compliant in tension. This is a result of the interatomic interaction becoming weaker at larger atomic separation. This is somewhat in

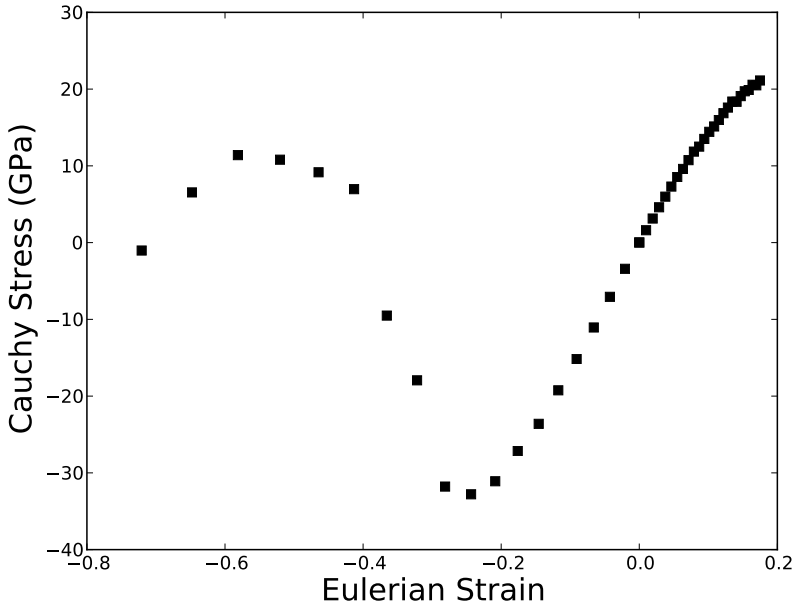

Figure 4.4: Cauchy stress as a function of Eulerian strain calculated using the Helmann-Feynman Theorem

contrast to polymer systems, which often stiffen in tension as polymer molecules are pulled straighter. Finally, there is an obvious jump in stress at a Green strain of about -0.2. This is likely an artifact of the fact that Si goes through as many as 10 phase changes between compressive stresses of about 12 GPa and 45 GPa [46]. Such phase transitions may lower the symmetry of the crystal structure and the four atom unit cell used here would no longer capture the true system behavior.

Figure 4.5 shows the volumetric material response: hydrostatic Cauchy stress as a function of dilatation. The same arguments about the stiffening in compressive volumetric deformation and becoming more compliant in tension can be made here as can be made about the uniaxial case.

We make the assumption that our strain energy can be decomposed additively

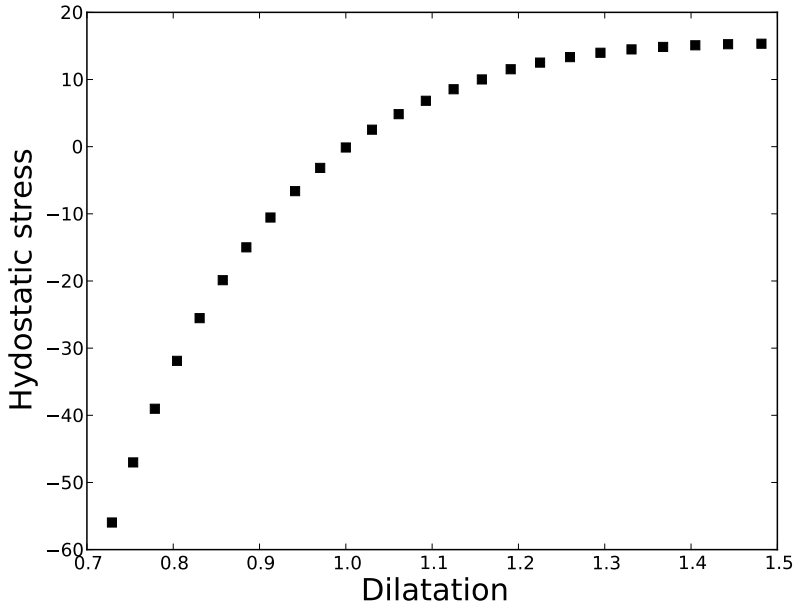

Figure 4.5: Hydrostatic Cauchy stress as a function of diliation

into deviatoric (tensile) and dilitational (volumetric) components,

$$W(\mathbf{F}) = W_{\text{tens}}(\lambda_{\langle 1\,\bar{1}\,0\rangle}) + W_{\text{vol}}(\det \mathbf{F})\,, \tag{4.12}$$

where $\lambda_{1\bar{1}0}$ is the stretch in the $\langle 1\,\bar{1}\,0\rangle$ direction. This is also the component of $\mathbf{F}$ associated with that direction. Both $\frac{dW_{\text{tens}}}{d\lambda_{\langle 1\,\bar{1}\,0\rangle}}$ and $\frac{dW_{\text{vol}}}{d\det \mathrm{F}}$ are monotonically increasing except for very large negative strains so W is strongly elliptic outside of those regions and a well posed constitutive law.

4.5 Implementation in Cosserat rod theory

We are now ready to implement this constitutive behavior into the framework of Cosserat rod theory, a fully nonlinear framework for slender rod-like objects [47]. In the static case where we assume the deformation is planar, the equilibrium

equations are

$$\frac{dV}{ds} + N\frac{d\phi}{ds} + \widehat{b}_2 = 0 \tag{4.13a}$$

$$\frac{dN}{ds} - V\frac{d\phi}{ds} + \widehat{b}_1 = 0 \tag{4.13b}$$

$$\frac{dM}{ds} + \xi V - \eta N + \widehat{g} = 0\,, \tag{4.13c}$$

where N is the axial force, V is the shear, M is the moment, $\widehat{b}_1$ and $\widehat{b}_2$ are applied body forces in the x_1 and x_2 directions, $\widehat{g}$ is an applied body couple, s is the position along the rod in the reference configuration, ϕ is the angle of the tangent of the deformed rod at s with respect to the x_1 axis, ξ is the axial stretch, and η is the shear strain. N, V, M, $\widehat{b}_1$, $\widehat{b}_2$, and $\widehat{g}$ are all per unit undeformed length. Since the rod is along the $\langle 1\,\overline{1}\,0\rangle$ crystal direction, $\xi = \lambda_{\langle 1\,\overline{1}\,0\rangle}$ from Equation (4.12). Here, we make the assumption of no body forces or body couples ($\widehat{b}_1 = \widehat{b}_2 = \widehat{g} = 0$) and that the rod is extensible but unshearable ($\eta = 0$). Constitutive relations are

$$N = \frac{\partial \Upsilon(\xi,\, \kappa)}{\partial \xi} \tag{4.14a}$$

$$M = \frac{\partial \Upsilon(\xi,\, \kappa)}{\partial \kappa} \tag{4.14b}$$

where κ is the curvature of the rod and $\kappa = \frac{\partial \phi}{\partial s}$. Because the bending stiffness is minimal in the structural response, bending response has been modeled as linear and tensile response as shown in Figure 4.3,

$$N = A\frac{\partial \Upsilon_{\text{tens}}(\xi)}{\partial \xi} = A\sigma(\xi) \tag{4.15a}$$

$$M = YI\kappa = YI\frac{d\phi}{ds} \tag{4.15b}$$

where Υ_{tens} is the energy shown in Figure 4.2 but as a function of ξ instead of Green strain, Y is the tensile tangent modulus around the stress free state, A is the cross sectional area, and I is the cross sectional moment of inertia. The cross section is rectangular, so $A = wt$ and $I = \frac{1}{12}wt^3$ where w is the width of the cross

section and t is the thickness. Comparing Equations (4.15) to Equations (4.14), Υ must be

$$\Upsilon(\xi,\, \kappa) = \frac{1}{2} Y I \kappa^2 + A \Upsilon_{\text{tens}}(\xi)\,. \tag{4.16}$$

One final difficulty is this rod theory assumes a prismatic rod and the beam being modeled has significant variation in width. This can be overcome by assuming Υ is a function of position along the beam s,

$$\Upsilon(\xi,\, \kappa;\, s) = \frac{1}{24} Y w(s) t^3 \kappa^2 + w(s) t \Upsilon_{\text{tens}}(\xi)\,. \tag{4.17}$$

Equations (4.15) become

$$N = w(s) t \frac{\partial \Upsilon_{\text{tens}}(\xi)}{\partial \xi} = w(s) t \sigma(\xi) \tag{4.18a}$$

$$M = \frac{1}{12} Y w(s) t \kappa = \frac{1}{12} Y w(s) t \frac{d\phi}{ds} \tag{4.18b}$$

and their derivatives are

$$\frac{dN}{ds} = \frac{dw(s)}{ds} t \sigma\left[\xi(s)\right] + t w(s) \frac{d\sigma\left[\xi(s)\right]}{ds} \frac{d\xi(s)}{ds} \tag{4.19a}$$

$$\frac{dM}{ds} = \frac{1}{12} Y t^3 \left[\frac{dw(s)}{ds} \frac{d\phi(s)}{ds} + w(s) \frac{d^2\phi(s)}{ds^2} \right] \tag{4.19b}$$

In preparation for input into a numerical differential equation solver, Equations (4.13) must be put in the form $\mathbf{x}' = f(\mathbf{x})$ where $\mathbf{x}$ is a vector of the independent variables to be solved for. To change Equation (4.13c) from a second order ODE to two first order ODEs we make the substitution $\zeta = \phi'$. Putting Equations (4.18)

and (4.19) into (4.13) and isolating all derivatives on the left, we get

$$V' = -wt\sigma\zeta \tag{4.20a}$$

$$\xi' = \frac{V\zeta}{wt\sigma'} - \frac{w'\sigma}{w\sigma'} \tag{4.20b}$$

$$\phi' = \zeta \tag{4.20c}$$

$$\zeta' = -\frac{w'}{w}\zeta - \frac{12V\xi}{Ywt^3} \tag{4.20d}$$

$$x_1' = \xi\cos\phi \tag{4.20e}$$

$$x_2' = \xi\sin\phi \tag{4.20f}$$

where all primes indicate differentiation with respect to s except σ is differentiated with respect to ξ. Equations (4.20e) and (4.20f) are included so that the deformed rod shape is solved along with the other variables.

Equations (4.20) are solved numerically using a Python wrapper of Fortran's BVP_SOLVER package for solving boundary value problems of ODEs. Because the beam and loading are symmetric, only half is explicitly included in the solution. The six boundary conditions for the six ODEs are

$$\phi(s=0) = 0,\ x_1(s=0) = 0,\ x_2(s=0) = -\delta \tag{4.21a}$$

$$\phi(s=L) = 0,\ x_1(s=L) = 0,\ x_2(s=L) = 0 \tag{4.21b}$$

Once a solution is achieved for a given δ value, the loading force is $V(s=0)$. An entire loading curve can be obtained by increasing δ from 0 to a maximum value and solving the BVP at each load step. The converged solution for one step is used as an initial guess for the next step.

BVP_SOLVER works by discretizing the first order ODE system using finite differences [48]. If we write Equations (4.20) as $\mathbf{x}' = f(\mathbf{x})$ we can approximate the derivate as $(\mathbf{x}_{i+1} - \mathbf{x}_{i-1})/(2h) = f(\mathbf{x}_i)$ where h is a step size in s. If this is done at

a number of points s_i, we get a system of nonlinear algebraic equations in terms of the values of $\mathbf{x}_i$ at s_i,

$$\mathbf{F}\left(\{\mathbf{x}_i\}\right) = \mathbf{0}\,. \tag{4.22}$$

BVP_SOLVER then solves this system of equations using a damped Newton method.

4.6 Cosserat rod model results

Figure 4.6 shows the deformed beam shape calculated from Equations (4.20) for a center deflection of 1.5 µm. The color of the line indicates average cross section stress in GPa. Qualitatively this looks quite similar to the results obtained from the anisotropic elastic finite element model in Figure 2.5. As expected, the stress is higher in region with smaller cross section.

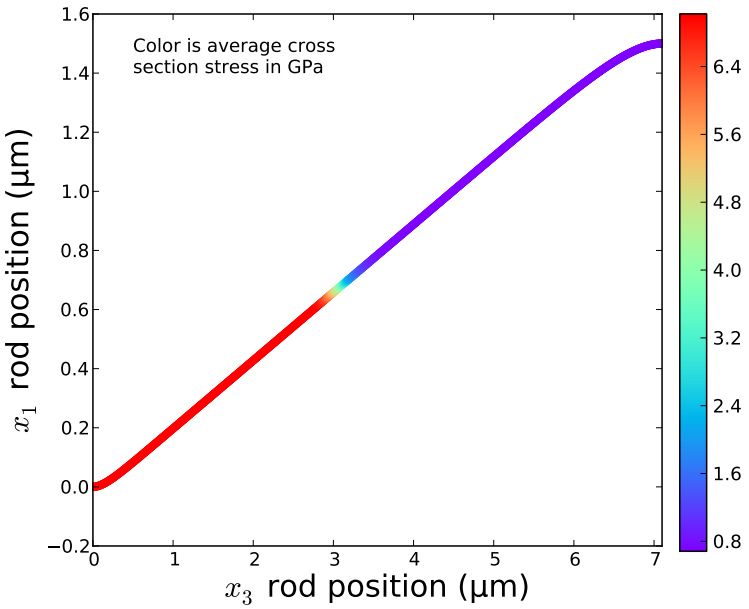

Figure 4.6: Deformed beam shape at a center deflection of 1.5 µm

Figure 4.7 shows the reaction force as a function of center displacement. Notice

how the membrane effect dominates the structural response so much that the initial, linear bending stiffness is not even visible.

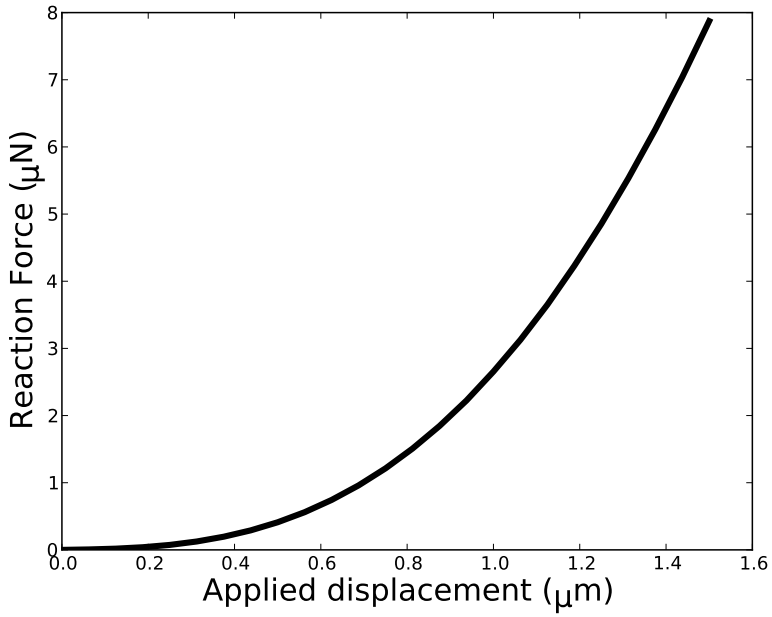

Figure 4.7: Reaction force as a function of center deflection

When stress is calculated, the most interesting quantity is the maximum stress occurring in the beam. This occurs at the center of the bottom of the beam, on the stretched side directly under where the force is applied. In order to calculate stress at a location other than the centerline we need to calculate the stretch at that location. To do this, assume we take a section of beam and first deform it to some stretch ξ and then bend it into a circular arc of radius R, as in Figure 4.8. The length of the deformed centerline is now $R\theta$ and it was initially $R\theta/\xi$. The length at the outside edge is now $(R + t/2)\theta$. The stretch $\lambda_{\max}$ is then

$$\begin{aligned} \lambda_{\max} &= \frac{(R + t/2)\theta}{R\theta/\xi} = \xi\left(1 + \frac{t}{2R}\right) = \xi(1 + t\kappa/2) \\ &= \xi(1 + t\phi'/2)\,. \end{aligned} \tag{4.23}$$

Stress can then be calculated using $S_{\max} = W'_{\text{tens}}\left(\lambda_{<1\bar{1}0>} = \xi(1 + t\phi'/2)\right)$. This is done as a function of center displacement and is shown in Figure 4.9

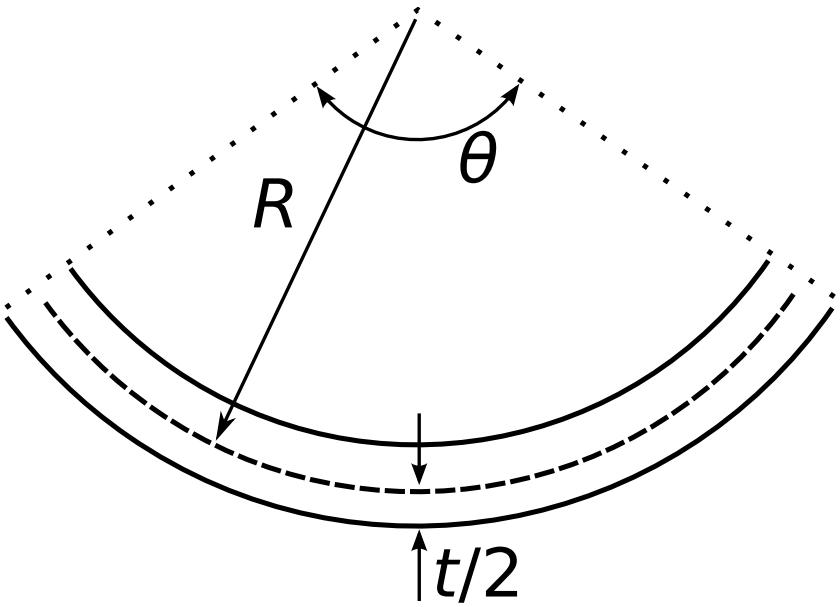

Figure 4.8: Diagram demonstrating the geometry involved in calculating the axial stretch at the edge of the cross section

In order to estimate the error resulting in calculating stress using a linear elastic material model rather than hyperelastic, the above calculations were repeated using a linear material response,

$$\Upsilon_{\text{lin}}(\xi,\, \kappa;\, s) = \frac{1}{24} Y w(s) t^3 \kappa^2 + \frac{1}{2} w(s) t Y (\xi - 1)^2 \,. \tag{4.24}$$

4.7 Constitutive model conclusions

Figures 4.10 and 4.11 show the reaction force and maximum stress using both the elastic and hyperelastic material models. While the two constitutive laws give slightly different force curves, they end up giving almost identical stresses. This is good news because while the rod theory model is good for comparing the effect of different constitutive laws, it cannot be used to compute fracture stresses from a real experiment. While the structural response of the beam deformation can be well modeled by rod theory, in the local area around where the force is applied,

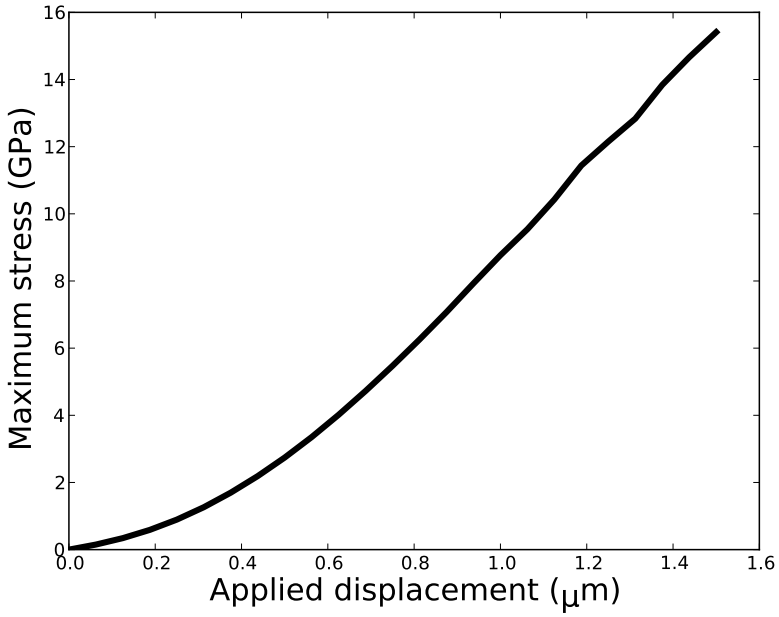

Figure 4.9: Maximum stress as a function of center deflection

additional bending occurs around the beam's axial direction, making the beam act more like a plate. This effect is negligible when computing the response of the entire beam but does contribute an extra stress component which rod theory would not account for. This case study demonstrates that even though the material experiences strains outside the material's regime of linear constitutive response, stresses can still be accurately calculated using an anisotropic elastic material model.

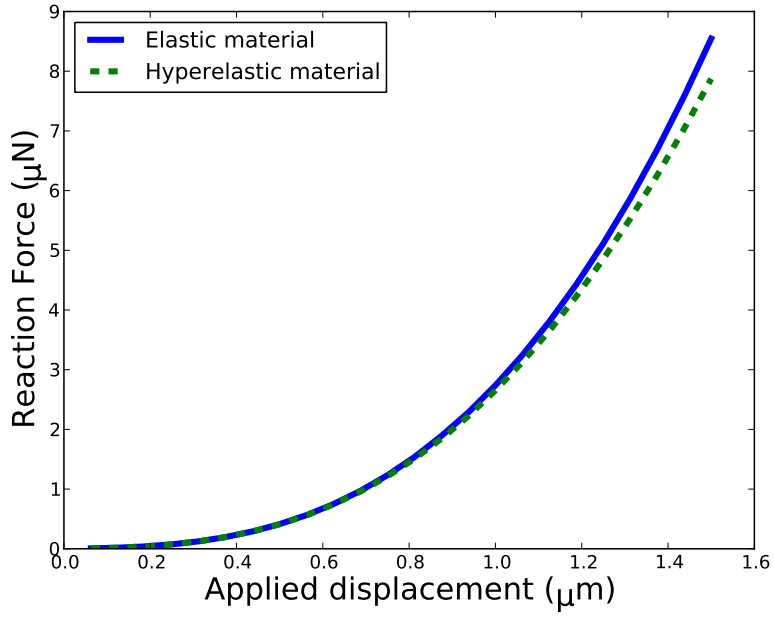

Figure 4.10: Reaction force as a function of center deflection calculated using both elastic and hyperelastic material models

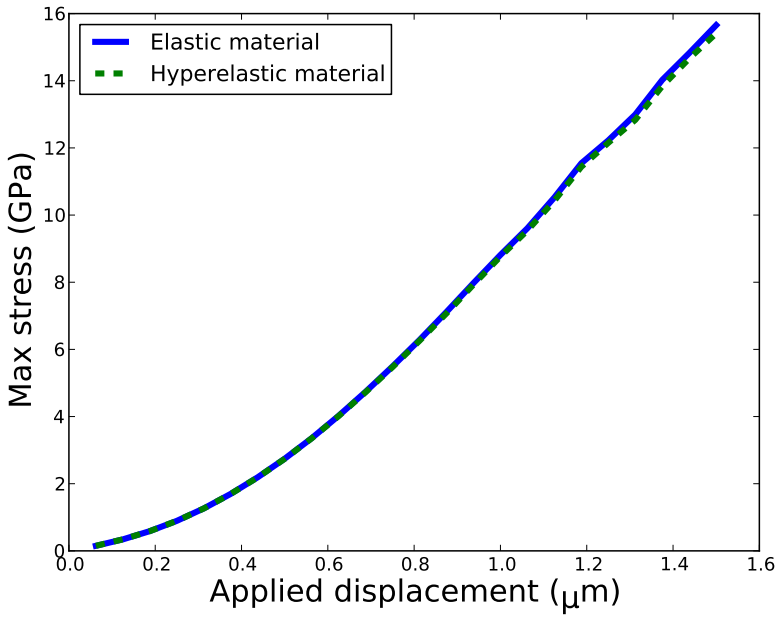

Figure 4.11: Maximum stress as a function of center deflection calculated using both elastic and hyperelastic material models

CHAPTER 5

ARXPS MEASUREMENT OF NATIVE OXIDE DEVELOPMENT

5.1 Film thickness measurement with XPS

Scanning tunneling microscopy (STM) based studies [49] have shown that initial oxidation of a Si (1 1 1) surface results in atomic scale roughening and that a complete monolayer is achieved after 400 hours, or about 17 days. No information is provided for the rate of this initial oxidation in less than saturated environments however. A quantitative description of the changes in coverage and thickness of the oxide layer over time in an unsaturated environment is a necessary piece of information for the development of an understanding of the mechanism by which oxidation affects strength of (1 1 1) oriented Si nanostructures.

A method of using x-ray photoelectron spectroscopy (XPS) to measure thick, artificially grown silicon dioxide layers on crystalline silicon is described by Lu, *et al.* [50]. Because Si in a pure, crystalline structure is in a different oxidation state than the Si in amorphous SiO_2, the energy of a $2p$ Si photoelectron is slightly different in each case. This difference can be easily resolved using XPS. The method of Lu, *et al.* [50] uses the intensity ratio of the crystalline Si $2p$ peak (I_{Si}) to the $2p$ peak from Si in SiO_2 ($I_{\mathrm{SiO_2}}$) to determine the thickness of the oxide layer ($d_{\mathrm{SiO_2}}$) by the equation

$$d_{\mathrm{SiO_2}} = \bar{\lambda}_{\mathrm{SiO_2}} \sin\alpha \ln\left[I_{\mathrm{SiO_2}} / \left(\beta I_{\mathrm{Si}}\right) + 1\right] , \tag{5.1}$$

where α is the photoelectron takeoff angle, $\bar{\lambda}_{\mathrm{SiO_2}}$ is the effective attenuation length of photoelectrons from the Si substrate through the SiO_2 film layer, and β is defined as $I_{\mathrm{SiO_2},\infty}/I_{\mathrm{Si},\infty}$, the ratio of the intensity of a SiO_2 peak from bulk SiO_2 to the intensity of a Si peak from bulk Si.

An improvement on the above method can be made through the use of angle resolved XPS (ARXPS) in conjunction with the quantitative analysis software QUASES-ARXPS[51]. In ARXPS, measurements are taken at a number of values of angle α and the film thickness is calculated to best fit all of the data.

5.2 Sample preparation

Native oxide films were grown on 1 cm × 1 cm chips cut from a single Si (1 1 1) wafer. Before oxidation, the chips were cleaned with a standard RCA procedure [52] consisting of 10 minutes at 70 °C in a 5:1:1 H_2O:H_2O_2:NH_4OH solution then 10 minutes at 70 °C in a 5:1:1 H_2O:H_2O_2:HCl solution. After cleaning, the samples were stripped of any SiO_2 with 30 seconds in 6:1 BOE. BOE was used instead of HF to produce a smoother H-terminated Si (1 1 1) surface [53]. Samples were aged in three environments: a "dry" environment of approximately 25 % relative humidity, a "wet" environment of approximately 100 % relative humidity, and the unaltered laboratory environment of approximately 60 % relative humidity (referred to as the "ambient" environment). ARXPS measurements of one set were taken at 1, 2, 3, 5, 1, 19, and 33 days of exposure. Spectra at exposure times longer than 33 days were inconclusive, likely due to increased carbon contamination.

5.3 ARXPS procedure and parameters

Samples were analyzed using a Surface Science Instruments SSX-100 with operating pressure of about 2×10^{-9} Torr. Monochromatic Al K-α x-rays (1486.6 eV [54]) were used with beam diameter of 1 mm and oriented at 55° relative to the sample

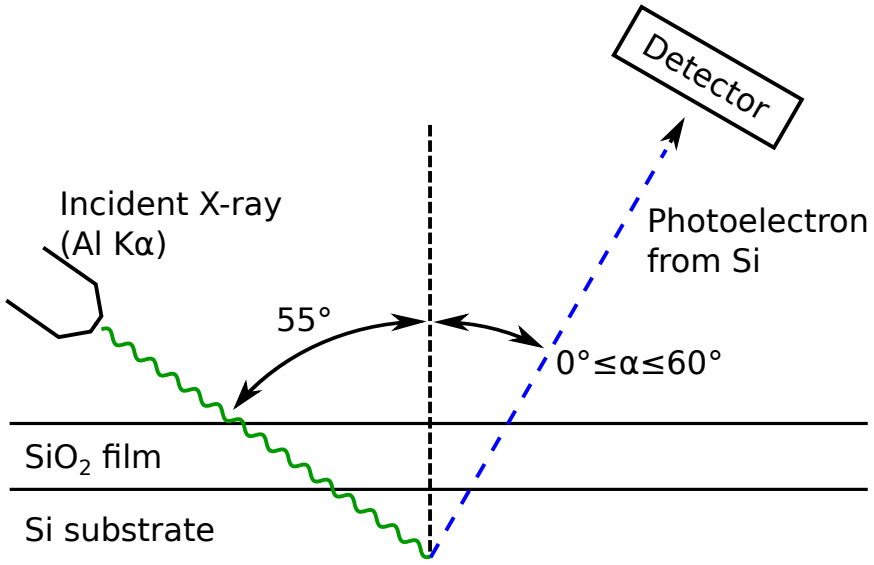

Figure 5.1: Schematic showing the geometry of the XPS experiment. The incident x-ray is shown causing a photoelectron to be ejected from the Si substrate which then is captured by the detector positioned at angle α.

normal. A hemispherical analyzer determined electron kinetic energy, using a pass energy of 150 V for wide/survey scans, and 50 V for high resolution scans. Spectra were taken with a binding energy range from 92 eV to 112 eV. The peaks of interest, the Si $2p$ peak from crystalline Si and the Si $2p$ peak from Si in amorphous SiO_2, have characteristic binding energies of 99.3 eV and 103.3 eV, respectively [55]. Spectra were taken at $\alpha = 0°$, $10°$, $20°$, $30°$, $40°$, $50°$, and $60°$. This geometry is shown in Figure 5.1.

CasaXPS software [56] was used to fit a Gaussian to each of the Si $2p$ and SiO_2 $2p$ peaks. The background photoelectron intensity was subtracted from each peak using the Shirley method [57] and the ratio of integrated intensities of the two peaks was recorded at each angular position. A representative spectrum from the 33 day wet environment sample at $0°$ and $60°$ is shown in Figure 5.2. A thicker SiO_2 layer would result in a larger SiO_2 peak. At higher values of angle α, photoelectrons from the Si will have to travel a longer distance through the SiO_2. This will have

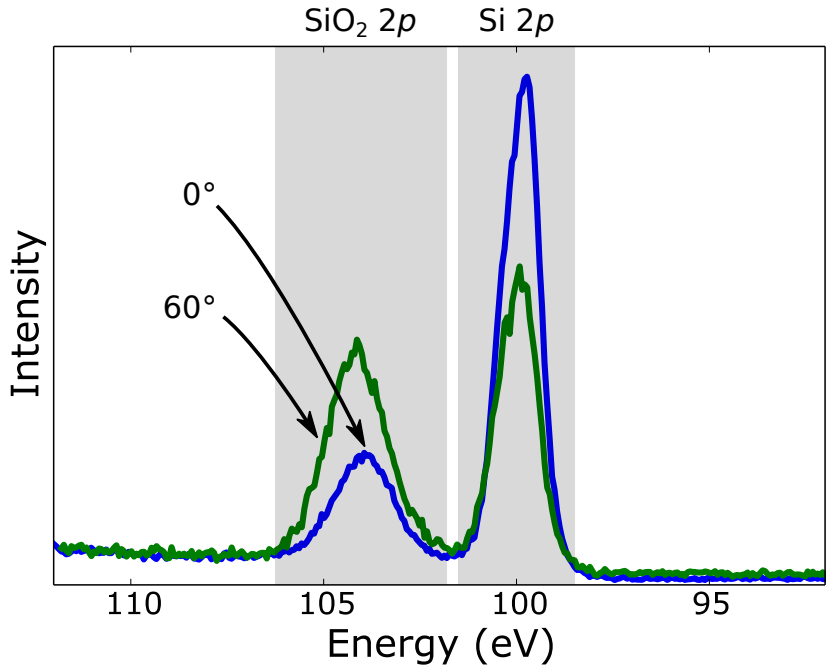

Figure 5.2: Representative XPS spectrum from the 33 day wet environment sample at $\alpha = 0°$ and 60° relative to the detector. Intensity units are arbitrary and not shown.

a similar effect on the resulting spectrum as a thicker SiO_2 layer. This can be seen in Figure 5.2, where the ratio of the SiO_2 peak to the Si peak decreases with increasing angle, α.

After acquiring the XPS spectra, the data was input into the quantitative analysis software QUASES-ARXPS. QUASES-ARXPS builds a simulated film stack taking physical characteristics of each film layer such as coverage, concentration, and thickness as parameters and calculates the intensity ratio of the SiO_2 to the Si peak as a function of angle, α. Experimentally unknown parameters are allowed to vary and an optimization routine is run to fit the generated data to the experimental. In this case, the coverage and concentration were fixed at 100 % and the thickness of the SiO_2 layer was allowed to vary. The QUASES-ARXPS software does not use the effective attenuation length as in Equation (5.1), but instead a similar quantity

Table 5.1: Inelastic mean free path values for photoelectrons at 99.3 eV and 103.3 eV through Si and SiO_2

	through Si	through SiO_2
$\lambda_{99.3}$	5.26 Å	7.68 Å
$\lambda_{103.3}$	5.36 Å	7.75 Å

called the inelastic mean free path (IMFP). The IMFP for photoelectrons at energies of 99.3 eV and 103.3 eV (corresponding to the Si $2p$ peaks from crystalline Si and amorphous SiO_2 respectively) through crystalline Si and amorphous SiO_2 were obtained from using the NIST IMFP database [58] using data from Tanuma, *et al.* [59] and are shown in Table 5.1.

5.4 Results

The SiO_2 average thickness values resulting from QUASES-ARXPS fitting to the experimental data are shown in Figure 5.3. The lines are a qualitative aid in visualization but are not intended to provide quantitative comparisons. In the QUASES-ARXPS fitting, coverage and film thickness have a very similar effect on photoelectron intensity and as a result fitting both the coverage and thickness of the simulated film to the experimental data is an ill conditioned problem, especially for film thicknesses which are small relative to $\lambda_{103.3} \cos\alpha$ [51]. A more effective approach is to assume coverage fixed at 100 % and calculate an effective, *average* value for film thickness. The sub-angstrom average thickness for the 2 samples with lower humidity can be interpreted as incomplete surface coverage.

From the data in Figure 5.3 we draw two main conclusions. First, the rate of oxidation in the wet environment case drops quickly at around 15 days. This suggests that in a saturated environment a monolayer of oxide is produced in about

2 weeks, providing partial passivation slowing future oxidation. This timeline agrees with the STM based studies of early stage Si oxidation in a humid environment [49]. With this in mind, we estimate from the change in oxidation rate that a complete oxide monolayer is achieved at 15 days, corresponding to an average thickness of approximately 1.6 Å. Since oxide thickness is small relative to $\lambda_{101.3} \cos \alpha$ we can approximate coverage and thickness as inversely related. Assuming a monolayer has an effective thickness of 1.6 Å, we can rescale the thickness data to express coverage, shown as a secondary axis in Figure 5.3. Unfortunately, due to carbon contamination issues, we were not able to capture the long term, asymptotic behavior of equilibrium SiO_2 thickness and time to reach equilibrium.

Second, in the wet environment the sample oxidizes much more quickly than in both dry and ambient environments. Even though the dry and ambient environments span quite a large range in relative humidity (25 % to 60 %), they differ little from each other. This suggests that atmospheric humidity affects the rate of natural oxidation mainly for very high humidity levels. The slow rate of oxidation of Si (1 1 1) surfaces in unsaturated atmospheric conditions means that the initial state of partial coverage exists for at least several months. This agrees with the timeline of strength evolution of silicon nanostructures aged in unsaturated environments as seen in Chapter 6.

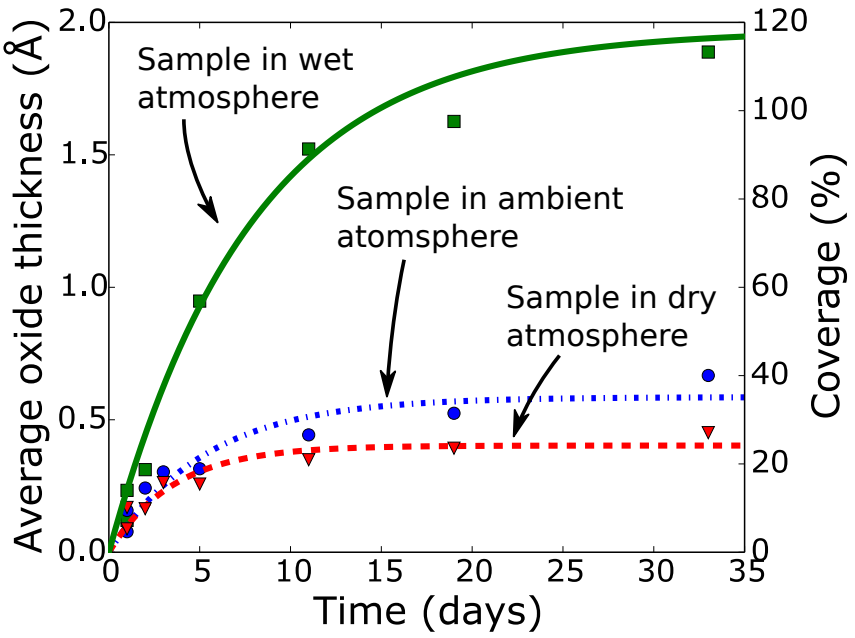

Figure 5.3: Transient average native oxide thickness for three levels of atmospheric humidity. Percent coverage is also shown assuming a complete monolayer is 1.6 Å thick.

CHAPTER 6

EFFECT OF OXIDE ON STRENGTH

6.1 Removal of oxide experiment

A set of experiments was designed to determine the mechanism by which oxidation affects strength of silicon nanostructures [60]. The first step was to prepare a set of nanobeam test specimens with H terminated surfaces. The H termination is unstable and oxidizes over a period of weeks to months. This natural oxidation is known as a native oxide and is well documented [61]. The beam specimens in question were allowed to oxidize over the course of one month while monitoring changes in strength. After this time, the oxide that had developed was removed with buffered oxide etch (BOE) and the strength was measured a final time. The results are shown in Figure 6.1 with the red circle data point showing the strength after oxide removal. The Weibull strength is used as the characteristic strength measure and error bars are 95 % confidence intervals.

There were two possible outcomes of the oxide removal experiment. If the strength had recovered after removing the oxide it would suggest that the presence of the oxide causes the strength change. If the strength did not recover it would suggest the oxidation process caused an irreversible change in the silicon surface which resulted in a strength change. Figure 6.1 shows that strength does not recover after oxide removal. This leads to the question what is the change that is occurring at the Si-SiO_2 interface? The most likely case is that oxidation induces an atomic scale roughening of the beam surface. Neuwald, *et al.* [49] used scanning tunneling microscopy to show that oxidation of an initially atomically flat Si (111) surface results in oxidation pits that form roughness on the order of single atomic steps.

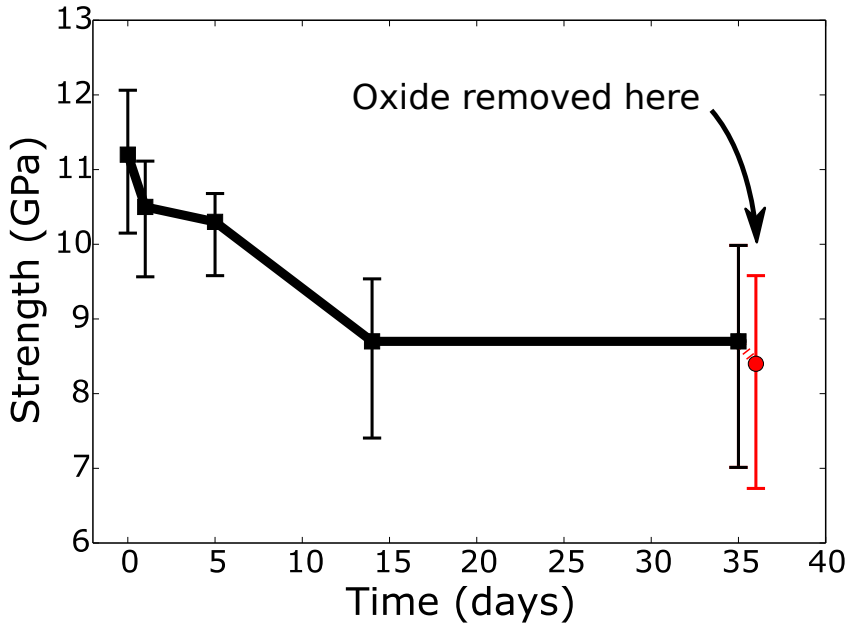

Figure 6.1: Results of oxide removal experiment with the final (red) data point being after the oxide is removed

In addition, Alan, *et al.* [12] showed that a similar level of roughness results in a strength change comparable to that seen in Figure 6.1. Chapter 5 discussed that in a humid environment a complete oxide monolayer forms in about 2 weeks, a timeline that agrees with Neuwald's STM based study, and that in atmospheres of low to moderate humidity the process is much slower, taking at least several months.

6.2 Strength of H terminated beams at longer times

Figure 6.2 shows the strength evolution of initially H terminated beams out through approximately one year. At first, strength decreases over the first several weeks in agreement with the trends in Figure 6.1. At longer times the strength stabilizes and then begins to increase, eventually recovering to a value within experimental

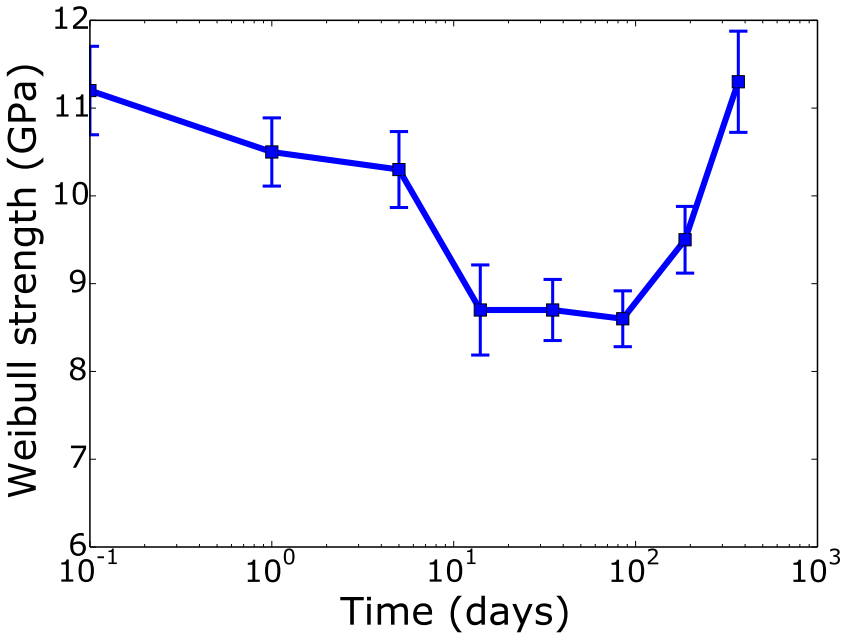

Figure 6.2: Strength evolution of initially H terminated beams out through approximately one year

uncertainty of the initial strength. This is at first a surprising result but will be explained in the coming sections.

6.3 Atomistic modeling of oxidation induced strength changes

In an effort to support our hypothesis that atomistic scale roughness can lead to significant strength changes, we used molecular dynamics to estimate the effect of small surface steps and partial oxidation on strength. The open source molecular dynamics code LAMMPS [62] was used with the inter-atomic interaction modelled by ReaxFF [63, 64]. ReaxFF parameters for Si and SiO_2 were obtained directly from Adri van Duin [65].

A semi-infinite crystalline silicon region was modelled with an amorphous oxide region at the free surface. The amorphous oxide structure was created following the procedure described by Van Duin, *et al.* [66] of initiating the oxide in an α-quartz structure, raising the temperature of the quartz region until it melted, then slowly cooling back to room temperature. The resulting SiO_2 structure is then annealed in an amorphous state. The system was deformed in displacement control while allowing stresses in orthogonal directions to relax. This was done with surface steps of various heights as well as surfaces partially terminated with a thin oxide and the remainder remaining in H termination. The latter case simulates the effect of the nucleation phase of the oxidation process on strength. Figure 6.3 shows the geometry of the partially oxidized surface simulation.

Figure 6.4 is representative of the failure in all cases and shows a crack initiating at a step of 6 atomic planes and propagating normally to the tensile direction. Figure 6.5 shows failure strength versus step height. Note that the relative strength decrease of approximately 25 % associated with small steps of 1–3 lattice planes is similar to the strength change seen in both our oxidation removal experiment and those by Alan, *et al.* [12]. Figure 6.6 shows failure as as a function of oxide nucleation fraction. Again, we see a relative strength change similar to the experimental data.

One unexpected feature of the failure modelled by ReaxFF seen in Figure 6.4 is that the oxide appears to be deforming ductilly across the crack that is forming in the crystalline silicon. It is possible that this is an artifact of the MD simulation, either a fault of the ReaxFF formulation itself or maybe the annealing process left the oxide structure in a metastable, kinetically frustrated state that exhibits unphysical ductility. It is also possible that an oxide in this essentially two dimensional geometry really does deform in a ductile manner. If that is the case, it may have

effects on strength beyond that of the oxidation induced roughening discussed earlier.

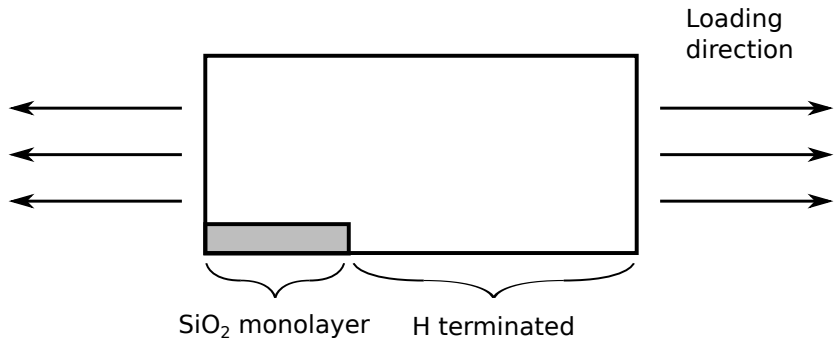

Figure 6.3: Schematic showing the geometry of the molecular dynamics simulation calculating the effect of partial oxidation of a silicon surface on strength. The simulation is periodic in both the loading and transverse directions.

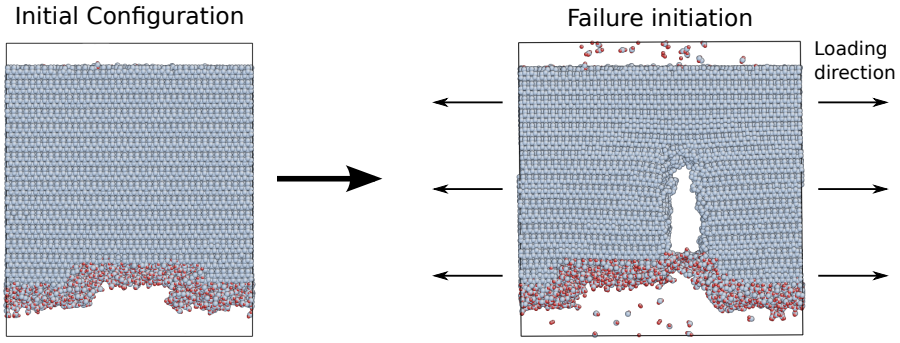

Figure 6.4: A cross section of a molecular dynamics simulation of effect of small surface steps on strength of oxidized surface. The initial configuration (after oxide formation) is shown on the left and the configuration just after failure initiation is shown on the right. The simulation shown involves a step height of 6 atomic planes and is qualitatively representative of all step heights.

6.4 Artificial oxidation experiments

In order to determine whether the ductile deformation of a thin oxide as predicted by ReaxFF MD is physically plausible or merely a numerical artifact, a set of beam

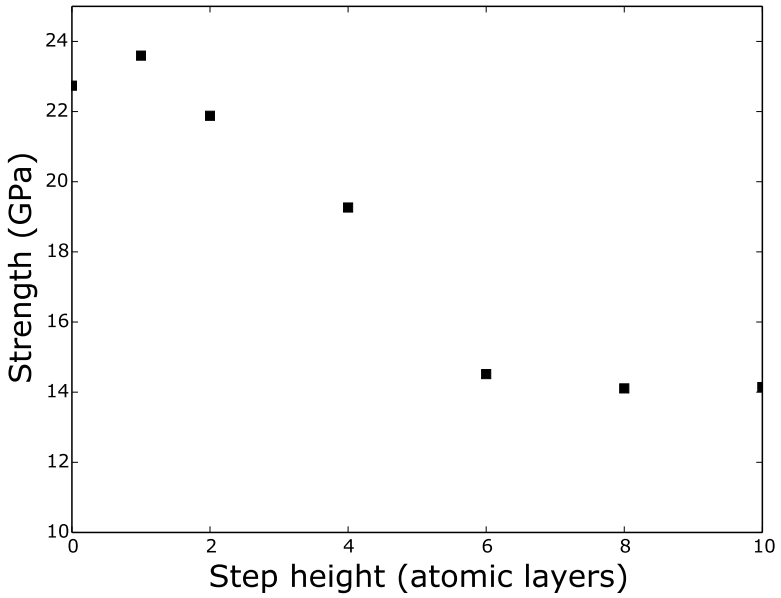

Figure 6.5: Failure stress as a function of height of surface step as calculated by ReaxFF MD

specimens was produced with oxides artificially grown to thicknesses in the range of 2 nm to 12 nm. A native oxide will naturally grow to about 2 nm but this will take at least several months in atmosphere with relative humidity less than 100 % as discussed in Chapter 5. Two methods were used to artificially grow an oxide similar to a naturally occurring native oxide. A thin and a thick oxide were grown with a rapid thermal processor (RTP) [67] and a thin oxide was grown with ozone exposure at room temperature and atmospheric pressure [68]. In all cases, oxide thickness was measured with ellipsometry [69]. Failure strength was measured twice: in the initial H terminated state and after oxide growth. The results are shown in Table 6.1. In all cases, experimental uncertainty is about 10 %.

In the cases of both the thin and thick RTP grown oxides, the strength after oxidation is higher than the initial strength. The strength increase, while consistent, is within experimental error in both cases. In the ozone assisted oxidation case

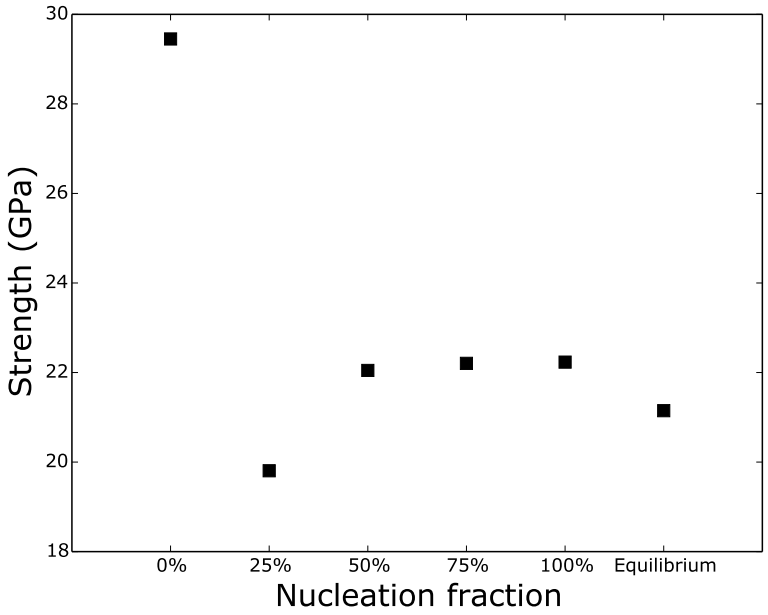

Figure 6.6: Failure stress as a function of oxide nucleation fraction on a flat surface as calculated by ReaxFF MD

Table 6.1: Strength results for artificially grown thin oxides. All experimental uncertainties are about 10 %.

	Pre-oxidation strength(GPa)	Post-oxidation strength (GPa)
RTP Thin (2.2 nm)	9.6	10.4
RTP Thick (11 nm)	10.7	11.4
Ozone (3 nm)	13.0	12.5

strength drops slightly but well within experimental error. The data suggests that although strength drops with initial oxidation, with more well developed oxides strength is maintained and perhaps even increased. One potential cause for this small strength increase is the ductile behavior seen in the MD simulations. Compressive stresses in the oxide could also be a cause but experiments show that the oxide film stress is much lower than the failure stresses seen here [70] and therefore not likely to be a major factor.

6.5 Parallel results from microscale, polysilicon experiments

Experiments performed at Sandia using the slack chain method [7] showing similar results are discussed here. The slack chain method is a high throughput testing approach that allows several hundred strength tests to be performed in a single day. The large number of data points allowed a detailed statistical analysis of the tensile strength distribution. The slack chain test specimens were fabricated using SUMMiT V [71] Reticle Set 723 with the tensile bars coming from the poly3 layer. In contrast to the single crystal nanobeam specimens, the slack chain specimens were polycrystalline and larger in size. The poly3 layer had a nominal thickness of 2.25 µm and the tensile bars had a nominal length of 20 µm and typical measured gage width of 1.9 µm. The strength data obtained using the slack chain method are displayed in Figure 6.7. All specimens were H terminated and stored in atmospheric conditions.

The data in Figure 6.7 are plotted in Weibull coordinates with the two parameter Weibull fit shown as the solid line. The Weibull strength parameters at 7, 29, and 761 days after release are shown in Table 6.2. Although these samples are of larger size and polycrystalline as opposed to single crystal, they track the same trend as the nanobeam specimens. At short times, strength drops but over longer times strength recovers to a value slightly higher than the original. Unlike the artificial oxidation strength data in Table 6.1, the high throughput aspect of the slack chain method allows for a large enough sample size that the these strengths are all statistically different to a 95 % confidence limit.

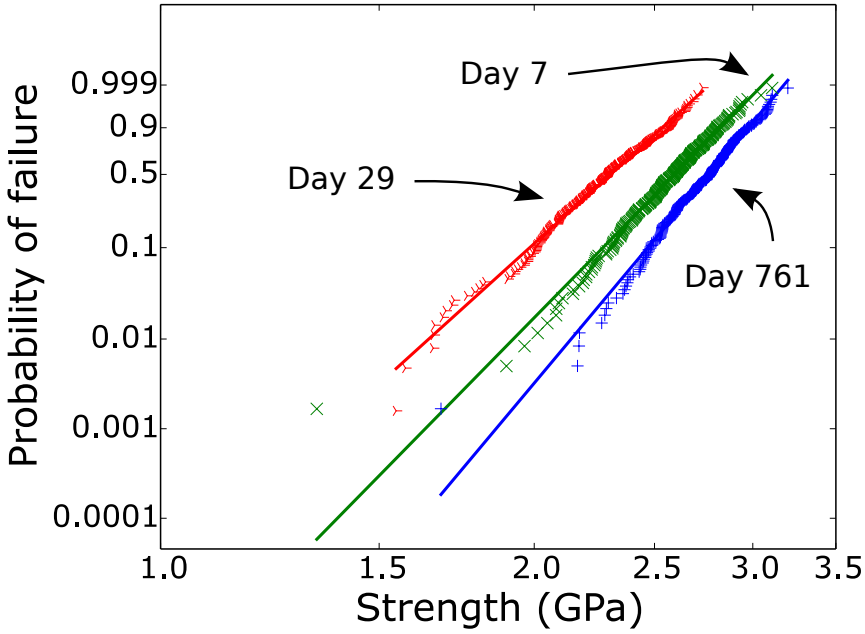

Figure 6.7: Strength data from microscale polysilicon specimens measured with the slack chain method [7] measured by Brad Boyce at Sandia National Laboratories

Table 6.2: Weibull strength values from slack chain method.

Time after release (days)	4	29	761
Weibull strength (GPa)	2.66	2.37	2.83

6.6 Summary

Atomic force microscope based experiments have shown that over a period of roughly one month the strength of initially H terminated Si nanostructures decreases by about 25 % with most of the change occurring within the first two weeks. This strength change can be shown to be a result of changes in the Si surface due to oxidation. By comparing the level of strength change to previous experiments which studied the effect of roughness on strength [12], and observing that scanning tunneling microscopy studies show that a similar roughness results from oxidation of an initially flat Si(1 1 1) surface [49], we conclude that the strength change

is a result of atomic scale roughness caused by oxidation. Molecular dynamics simulations corroborate this by showing similar strength decrease with small surface steps and partial oxidation of a simulated Si(1 1 1) surface. Molecular dynamics also suggests an unexpected ductile behavior in the oxide layer. Experiments with artificial oxides similar to fully developed native oxides show no strength decrease and perhaps a slight strength increase. We suggest that the initial oxide induced roughening is a transient effect of the oxidation front nucleating through each atomic layer and in equilibrium this oxidation front flattens. With the flattening, strength recovers with some indication that the fully developed oxide causes the structure to be slightly stronger than in its original state. Similar results are seen in the Sandia polysilicon structures when the strength dropped over short times but recovered when fully oxidized. Future work could include measuring oxidation induced roughness changes in specimens aged along with strength specimens as well as making more statistically significant measurements of strength increase with well developed oxide layers. Due to the small relative strength change, this would likely require a high throughput method like the slack chain in order to reduce statistical uncertainty.

CHAPTER 7

OXIDATION INHIBITION WITH SAMS

7.1 Motivation and previous results

In Section 1.2, it was mentioned that Alan , *et al.* [13] demonstrated a correlation between oxidation of Si (1 1 1) surfaces and a decrease in strength. They did this by observing that a set untreated, H terminated Si beam specimens similar to those used in this work oxidized over a period of 23 days, strength decreased from 16.2 GPa to 11.1 GPa. A second set of beam specimens was prepared with the H termination at the (1 1 1) surface replaced by a more stable methyl (CH_3) group. The two sets of beams were kept in identical environmental conditions and while the H terminated beams weakened by about 30 % the CH_3 terminated beams did not change beyond experimental error. The mechanisms behind this relation were discussed in detail in Chapter 6. We also made an effort to expand the study of the effect of organic surface coatings on strength evolution by looking at longer time scales and more coating materials. In addition to the H and CH_3 terminated beams, Cl terminated beams and those coated with silane monomers of chain length C_5 and C_{18} were also studied. The longer chain monomers form an approximately self assembled monolayer (SAM) and as such these beams are described here as "SAM coated". The SAM coated beams were aged through a period of 1 year while the Cl and CH_3 terminated beams were aged to 9 months.

7.2 Cl and CH_3 terminated beam specimens

7.2.1 Chlorination and methylization reactions

To prepare the Cl and CH_3 coated samples, beam specimens fabricated as described in Section 2.1. After the removal of the protective oxide layer, the beams were immediately placed in an inert atmosphere to prevent any oxidation of the H terminated surface. The samples were then exposed to 50 Torr of Cl_2 gas for 1 min. The Cl_2 was then purged and the samples were again exposed to more Cl_2, this time at 150 Torr for 20 min. This process replaced all the H termination of all Si surface sites with a Cl termination. Some samples were then removed for the Cl terminated strength tests.

The methylization reaction was achieved by refluxing the now Cl terminated with a methyl Grignard reagent (3 M CH_3MgCl in THF, Sigma Aldrich) under a constant flow of Ar gas for 4 hours. After the reaction, the samples were rinsed twice in anhydrous methanol and once in ultrapure water. The fidelity of both the Cl and CH_3 terminated Si surfaces were verified with Fourier transform infra-red spectroscopy (FTIR) [72].

7.2.2 Cl and CH_3 strength results

The Weibull strength as a function of time since surface functionalization for Cl and CH_3 coated samples along with a H terminated control are shown in Figure 7.1

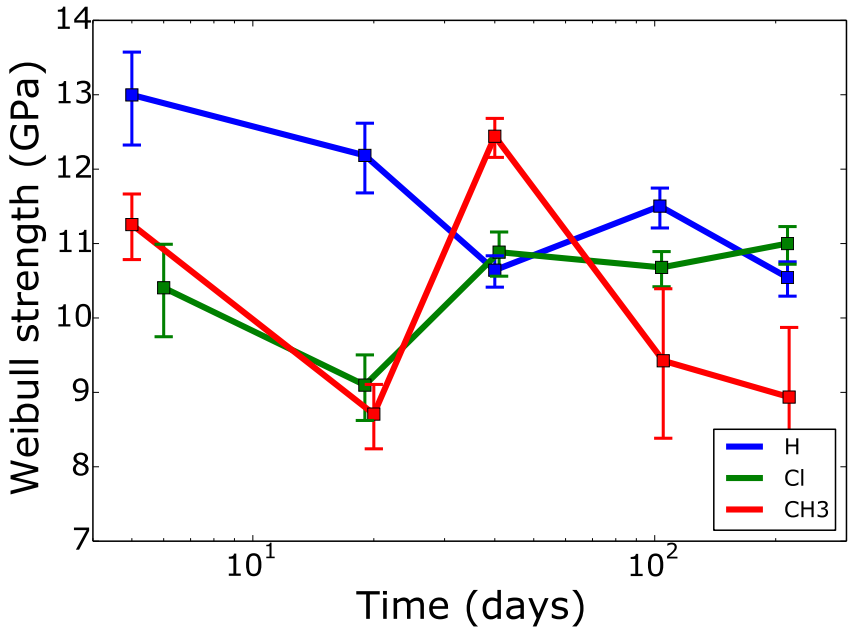

Figure 7.1: Strength results for Cl and CH_3 terminated samples with a H terminated reference sample

7.3 SAM coated beam specimens

7.3.1 SAM coating reaction

To prepare the SAM coated samples, the beam specimens were fabricated as described in Section 2.1. Two types of SAM coated samples were produced: with and without chemically oxidizing the H terminated Si surface before SAM deposition. The UV-O_3 grown chemical oxide may induce a slight compressive stress in addition to resulting in more complete silanization of the surface producing SAMs that are more robust and densely packed than their non-oxide counterparts [73]. As discussed in Chapter 6, any residual stress in the SiO_2 layer is small and unlikely to affect fracture strength of the beam specimen as a whole. First, all samples were cleaned for 10 min in an initially room temperature 1:1 piranha solution. Those

samples to be oxidized were then subjected to re-oxidation via an ultraviolet ozone (UV-O_3) treatment for 10 minutes, leading to the growth of a chemical oxide of with thickness of 1.3 nm as measured by spectroscopic ellipsometry.

Following the re-oxidation step, both chemically oxidized and H-terminated samples were immersed in 2 mM n-alkylsilane solutions of 3:2 hexadecane and carbon tetrachloride in a glovebox with a relative humidity of approximately 8%. Alkylsilanes of $n = 5$ were obtained from Santa Cruz Biotechnology (Santa Cruz, CA) and those of $n = 18$ from Sigma Aldrich (Milwaukee, WI). Both chemically oxididized and H terminated samples were allowed to react with the SAM solution for 90 minutes. Upon removal from the SAM solution, the samples were rinsed in fresh hexadecane:carbon tetrachloride solvent, isoproponal, and then dried under a stream of dry N_2. This resulted in highly hydrophobic SAM surfaces with water contact angles approaching 98.0 and 107.7 for $n = 5$ and $n = 18$ oxidized surfaces, respectively. Non oxidized samples exhibited slightly lower water contact angles due to the absence of a well-formed oxide layer for covalent siloxane bonding with angles reaching a maximum of 92.9° and 103.3° after 24 hours for $n = 5$ and $n = 18$, respectively.

7.3.2 C_5 and C_{18} silane strength results

The Weibull strength as a function of time since surface functionalization for samples coated with C_5 and C_{18} SAM with and without the initial SiO_2 layer and a H terminated control are shown in Figure 7.2.

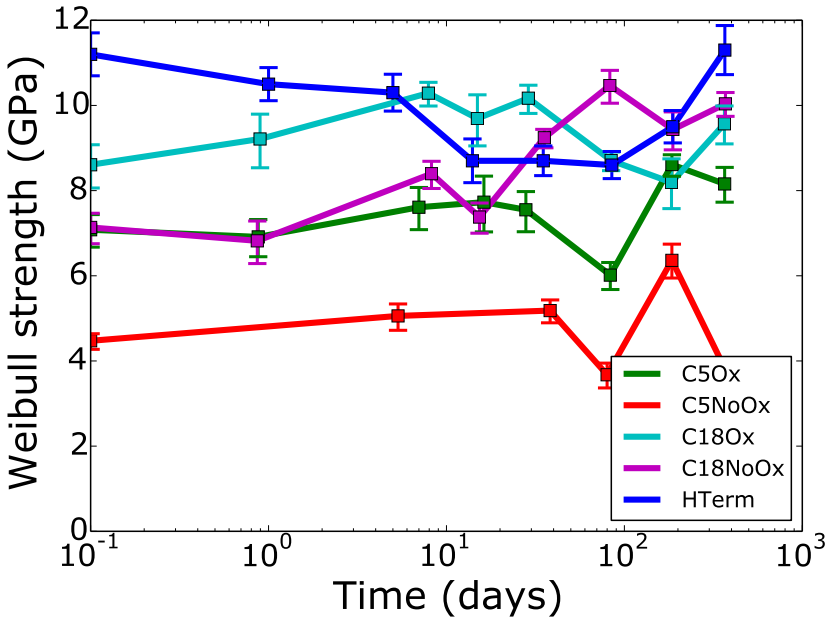

Figure 7.2: Strength results for C_5 and C_{18} SAM coated samples with a H terminated reference sample

7.4 Conclusions

Unfortunately, the results are not very conclusive for either the CH_3 or the SAM coated beams. In both cases, the strength of the H terminated sample drops rapidly, then stabilizes, then slowly recovers. This agrees with the trends discussed in Chapter 6. The strengths of the CH_3 and all SAM coated samples has much more scatter, beyond what we predict with the error analysis discussed in Section 2.5.3. The increased scatter makes it difficult to determine a trend. The Cl has a similar trend to the H terminated sample, as expected, though again with more scatter than expected.

The common factor between the CH_3 and the SAM coated samples is that all were subjected to a wet chemistry process after the protective oxide was removed. Even though efforts were made to keep the both reactions as clean as possible, an

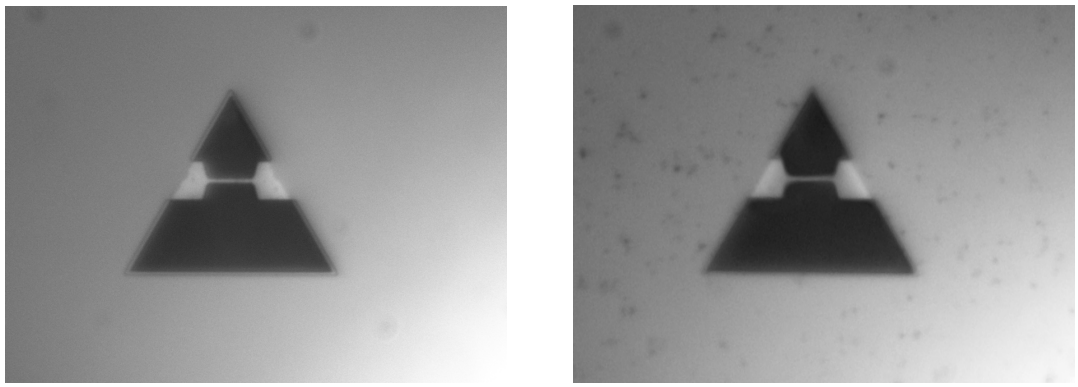

(a) (b)

Figure 7.3: Optical micrographs of an H terminated sample (a) and a C_5 SAM coated sample (b)

optical inspection of the CH_3 and SAM coated samples reveals they have a much dirtier surface than the H terminated samples. The Cl terminated sample is cleaner than those with organic coatings but still slightly dirtier than the H terminated samples. Figures 7.3a and 7.3b show optical microscopy images of an H terminated sample chip and a C_5 SAM coated chip and the difference in surface contamination between them. Qualitatively, there appears to be a relation between the cleanliness of the surface of the beam specimens and the scatter of the strength measurements. This is not entirely surprising considering the forces and displacements involved with these strength tests are small enough that any contamination between the AFM cantilever tip and the sample surface is likely to have an effect on the results.

APPENDIX A

FEA MESH DEVELOPMENT AND CONVERGENCE

As discussed in Section 2.3, a finite element model of the nanobeam specimens was was used to convert the force at failure measured with AFM to a stress at failure. Because the structure is symmetric, only half was directly simulated with symmetry conditions applied at the beam's center. The converged mesh is shown in Figure A.1a with Figure A.1b showing a closer view near the point of load application. C3D10 10 node quadratic continuum elements were used throughout the entire model.

To study convergence, the maximum stress was calculated with several meshes of increasing density and the results are shown in Figure A.2. Mesh number is a seeding parameter used when generating the model with higher mesh number corresponding to higher mesh density. The seeding of meshes 2–8 were directly proportional to the seeding parameter so that mesh 4 has twice the seed density as mesh 2. The geometry of mesh 1 was slightly changed to allow for extra corsening. Mesh 6 was considered converged and was used for all calculations. The model thickness was slightly changed to match the thickness calculated from the measured resonant frequency (described in Section 2.4) so that the resulting stress-force relation was accurate for that specific set of beams. No additional convergence tests were performed for these small modifications.

Load was applied in the model in displacement control over a circular area of diameter 20 nm at the center of the beam. The actual AFM tip contact area in the experiments was unclear because each tip wears differently but was estimated with SEM to be around 10 nm. Attempts were made to apply load in the model over a circular area of 10 nm and with a rigid spherical indentor with diameter 10 nm

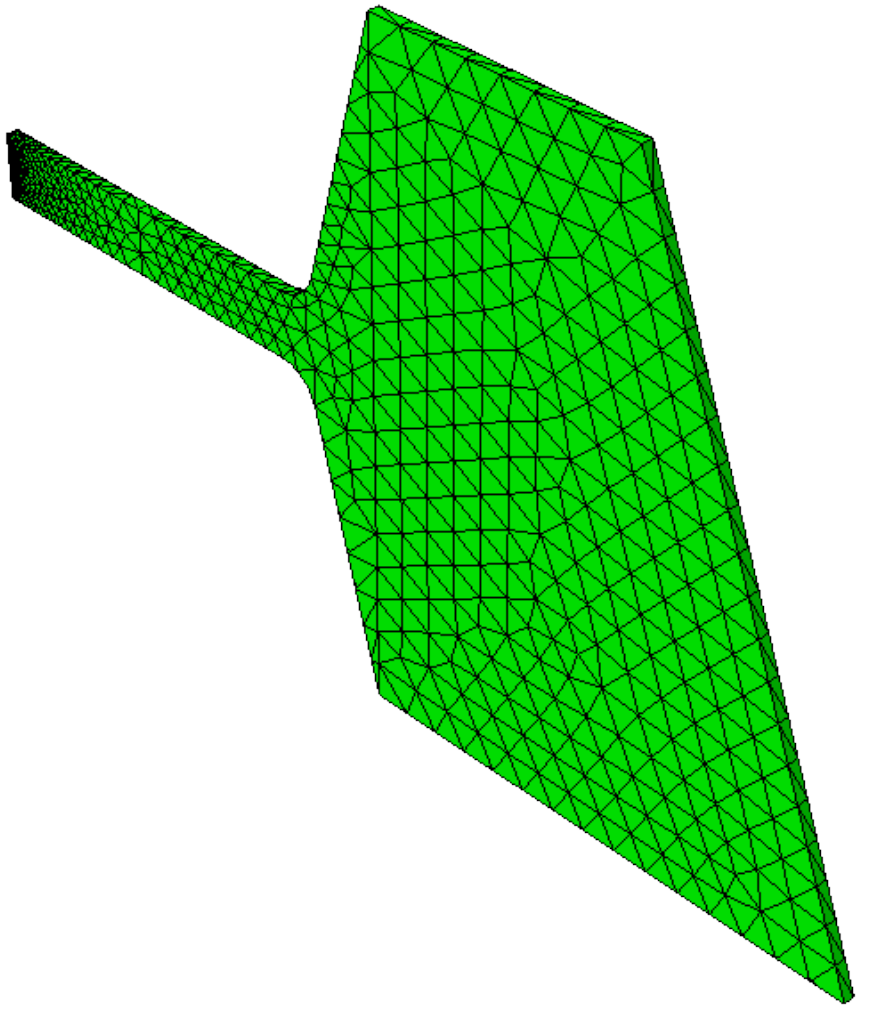

(a)

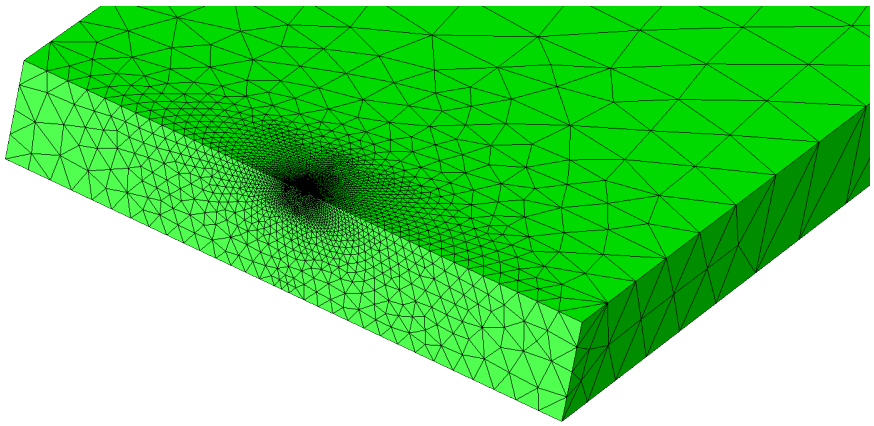

(b)

Figure A.1: Whole model mesh (a) and mesh geometry near load application (b) for mesh 6

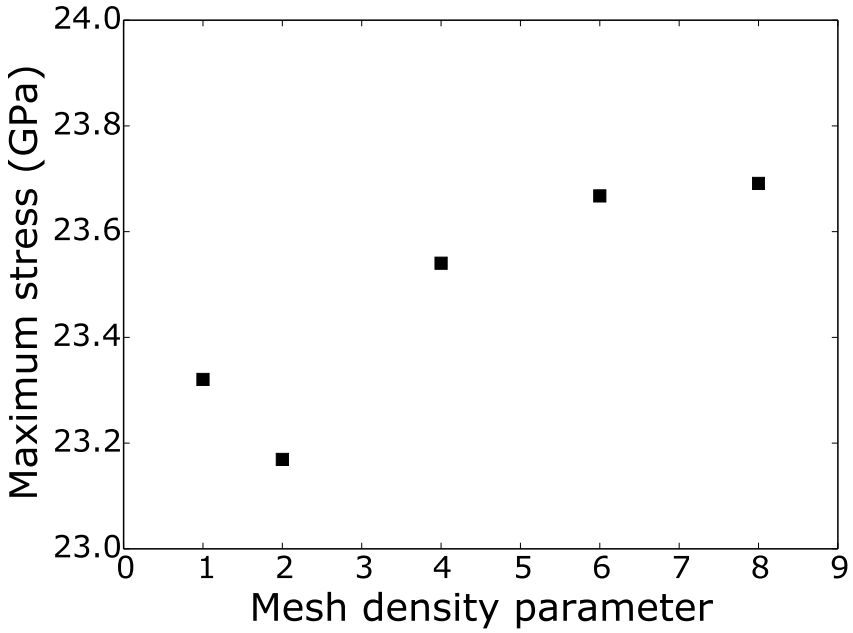

Figure A.2: Convergence testing for the finite element mesh shown in Figure A.1

but in both cases the model failed to converge beyond about half the maximum displacement. Saint-Venant's principle suggests that because all three of these loading cases are statically equivalent and the loading area is small compared to the rest of the beam geometry the difference in their effect on both structural response and maximum stress will be negligable. Figures A.3 and A.4 show the maximum stress as a function of displacement and applied force and support the accuracy of using the a displacement boundary condition over a 20 nm area. This also demonstrates that uncertainty in the AFM tip shape does not lead to additional uncertainty in stress.

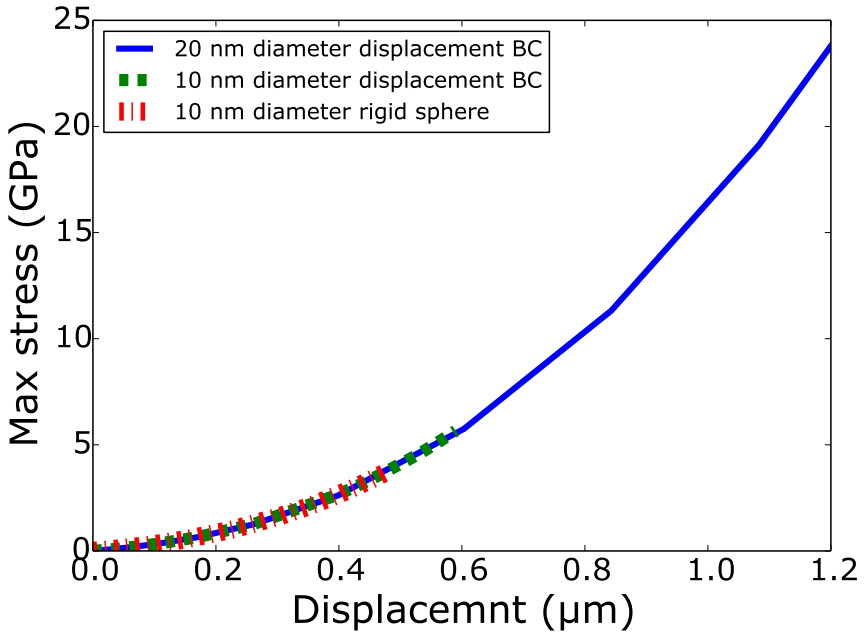

Figure A.3: Maximum stress as a function of applied displacement with the three different loading methods

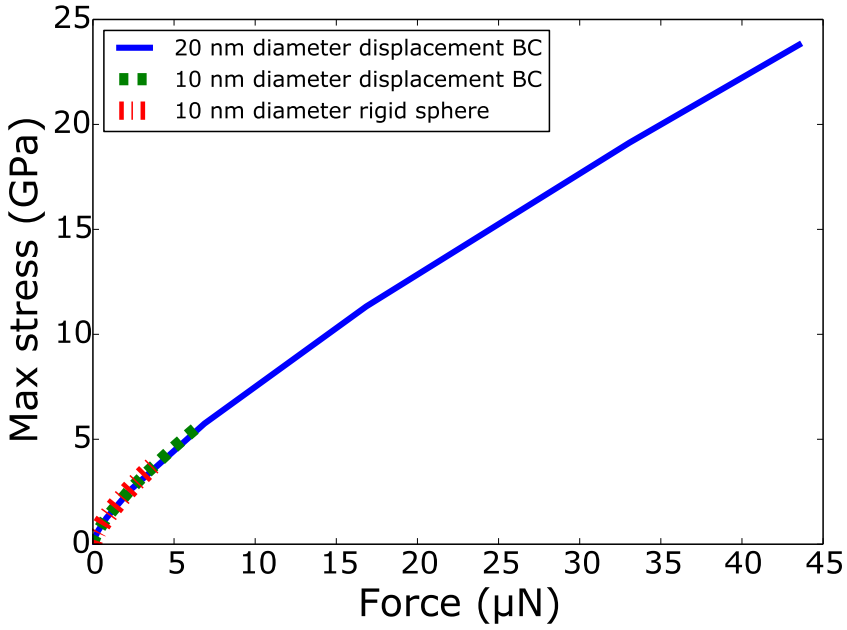

Figure A.4: Maximum stress as a function of applied force with the three different loading methods

APPENDIX B

DFT MODELING PARAMETERS

There are three convergence tests that need to be performed when starting a DFT simulation, the first being kinetic energy cutoff. A higher cutoff energy includes more terms from the plane wave basis in approximating φ. In order to determine what cutoff energy is sufficient for accurate results, several calculatations are run with a range of cutoff energy values. For some cutoff energy, the ground state energy will have converged and further increases in cutoff energy have little effect. The results of this process for the four atom Si lattice used in Chapter 4 are shown in Figure B.1. A cutoff energy off 100 Ry was used for all DFT calculations in Chapter 4. A Rydberg (Ry) is a unit of energy commonly used with atomistic calculations and corresponds to the ground state of a hydrogen atom. The value of 100 Ry was chosen somewhat conservatively to account for the fact that a larger cutoff energy will be required for unit cells in a highly strained state.

In addition, convergence with respect to the k-points needs to be assured. K-points are the numerical quadrature points in the wave vector space (k space) used to calculate the integral in Equation (4.4). The number and distribution of these points can affect the result of the calculation. In the unit cell investigated here, the $\langle 0\,0\,1\rangle$ dimension is $\sqrt{2}$ times the $\langle 1\,1\,0\rangle$ and $\langle 1\,\bar{1}\,0\rangle$ dimensions. Because the k-points discretize the reciprocal lattice space instead of physical space, there needs to be fewer k-points in the longer physical dimension, in this case $\langle 0\,0\,1\rangle$. Figure B.2 shows convergence of ground state energy with respect to number of kpoints in the $\langle 1\,1\,0\rangle$ and $\langle 1\,\bar{1}\,0\rangle$ directions. For the DFT calculations in Chapter 4, a k-grid of $10 \times 10 \times 8$ was used.

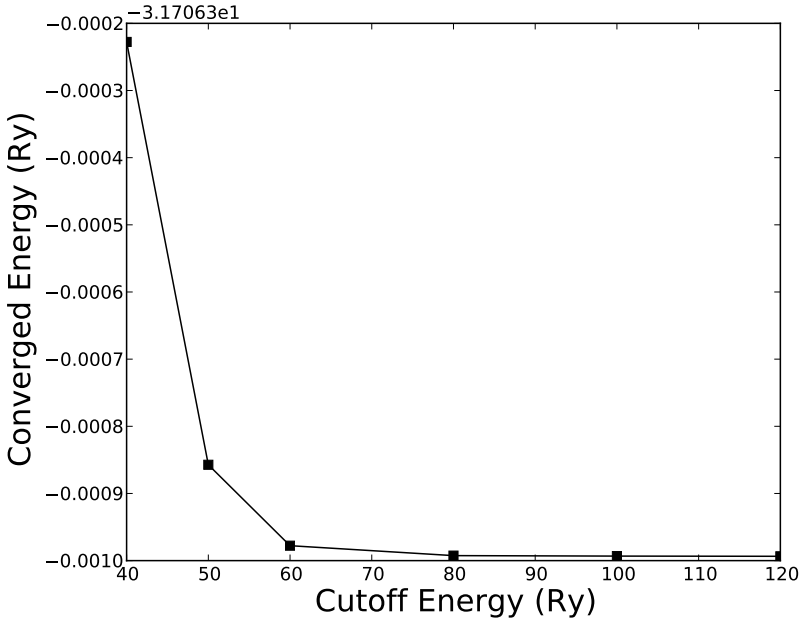

Figure B.1: Convergence of ground state energy of the 4 atom Si unit cell with respect to cutoff energy

Finally, the size of the unit cell is varied to find that which provides the minimum ground state energy and thus the relaxed crystal configuration. Ground state energy as a function of lattice parameter is shown in Figure B.3. The lattice parameter that minimizes energy is 10.21 Bohr while the accepted experimental value is 10.26 Bohr. A Bohr is a unit of length commonly used in atomistic calculations that corresponds to the radius of a hydrogen atom. This lattice parameter of 10.21 Bohr was used as the strain free state in Chapter 4.

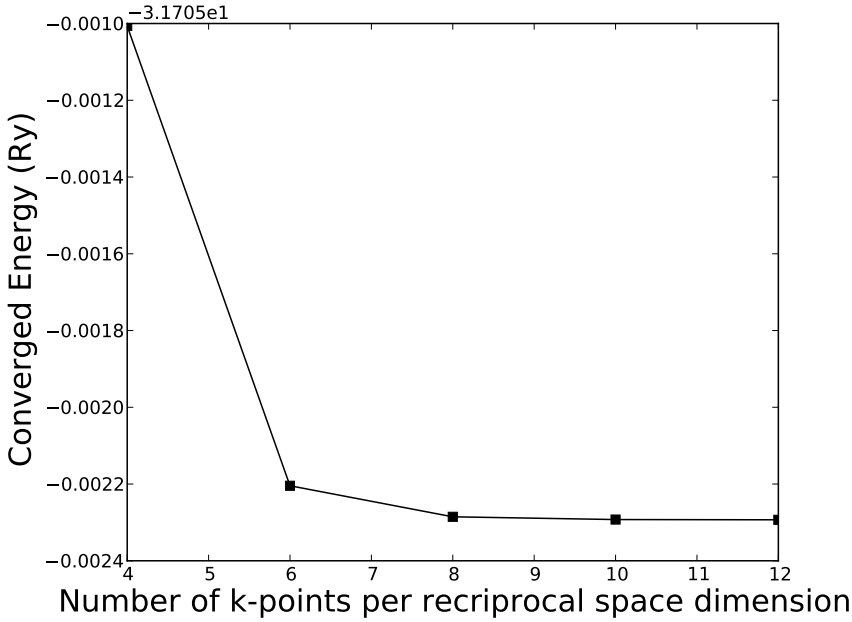

Figure B.2: Convergence of ground state energy of the 4 atom Si unit cell with respect to grid of k-points

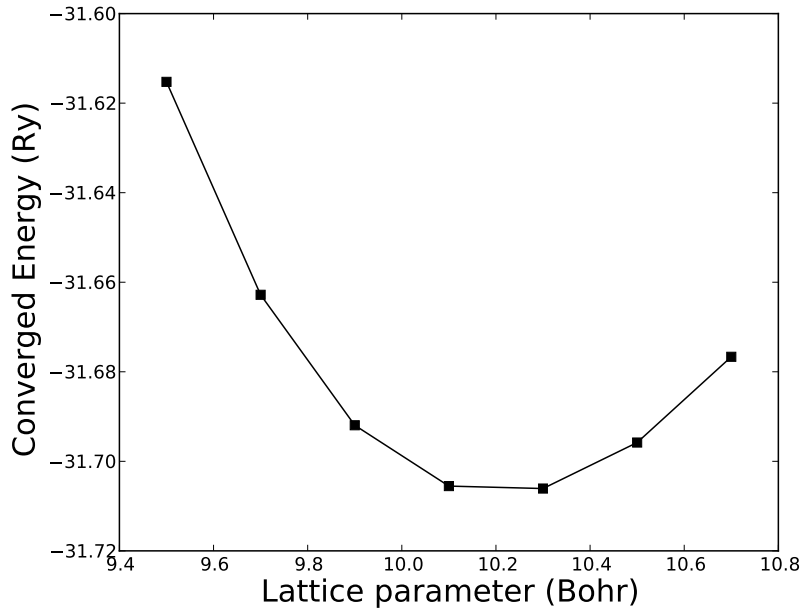

Figure B.3: Ground state energy of the 4 atom Si unit cell as a function of lattice parameter

APPENDIX C

REAXFF MD PARAMETERS AND BENCHMARKING

All molecular dynamics (MD) simluations were performed using the open source Large-scale Atomic and Molecular Massively Parallel Simulator (LAMMPS) [62] and the ReaxFF interatomic potential [63, 66]. The Stillenger-Weber and environment-dependent interatomic potential (EDIP) models have been shown to result in unphysical crack tip blunting and plasticity when simulating Si fracture [74]. The modified embedded atom method (MEAM) produces more physically realistic deformation around the crack tip and stress intensity factors matching experiments [74] but the LAMMPS implementation does not include parameters for O. ReaxFF has been shown to accurately simulate Si fracture [64] and the ability to produce a realistic SiO_2 structure [66]. ReaxFF parameters for silicon oxide systems were obtained directly from Adri van Duin (creator of ReaxFF) [65]. The ReaxFF parameters as formatted for input into LAMMPS are shown below.

To ensure physical accuracy of the MD model it was benchmarked by calculating the elastic moduli of Si. A fully periodic Si crystal was initialized with all other simuation parameters the same as in Section 6.3. Tensile and compressive modes of deformation were prescribed from the initial configuration corresponding to each strain component and the stress was calculated in each state. A single mode of deformation gave 12 moduli values. For example, a prescribed normal strain in the 1 direction gave 2 values, one compressive and one tensile, for each of the 6 C_{1j} components. The C_{ij} components in Table C.1 are the average of all compressive and tensile moduli from all prescribed deformation modes. All ReaxFF calculated moduli are shown in Table C.1 and agree with accepted values to within 4 %.

Table C.1: ReaxFF calculated Si elastic moduli compared to accepted values as a benchmark for accuracy of Si crystal deformations in ReaxFF

C_{ij}	Accepted value (GPa) [15]	ReaxFF value (GPa)	ReaxFF error
C_{11}	165.77	159.73	$-3.65\,\%$
C_{22}	165.77	159.73	$-3.65\,\%$
C_{33}	165.77	159.73	$-3.65\,\%$
C_{44}	79.619	78.490	$-1.42\,\%$
C_{55}	79.619	78.490	$-1.42\,\%$
C_{66}	79.619	78.490	$-1.42\,\%$
C_{12}	63.924	65.657	$2.71\,\%$
C_{13}	63.924	65.657	$2.71\,\%$
C_{23}	63.924	65.657	$2.71\,\%$
C_{14}	0.0	-3.28×10^{-8}	NA
C_{15}	0.0	1.11×10^{-9}	NA
C_{16}	0.0	3.58×10^{-9}	NA
C_{24}	0.0	1.92×10^{-9}	NA
C_{25}	0.0	4.19×10^{-8}	NA
C_{26}	0.0	6.10×10^{-9}	NA
C_{34}	0.0	-3.99×10^{-9}	NA
C_{35}	0.0	1.41×10^{-9}	NA
C_{36}	0.0	4.51×10^{-8}	NA
C_{45}	0.0	3.90×10^{-7}	NA
C_{46}	0.0	3.88×10^{-8}	NA
C_{56}	0.0	-4.26×10^{-8}	NA

```
Reactive MD-force field, Buehler PRL 2006, 2007 with oxygen (Neyts et al. JPC-C
    -2011)
 39       ! Number of general parameters
   50.0000 !Overcoordination parameter
    5.5469 !Overcoordination parameter
   21.2839 !Valency angle conjugation parameter
    3.0000 !Triple bond stabilisation parameter
    6.5000 !Triple bond stabilisation parameter
    1.0000 !Not used
    1.0159 !Undercoordination parameter
    9.0000 !Triple bond stabilisation parameter
    8.0878 !Undercoordination parameter
   13.0238 !Undercoordination parameter
  -13.8107 !Triple bond stabilization energy
    0.0000 !Lower Taper-radius
   10.0000 !Upper Taper-radius
    2.8793 !Not used
   33.8667 !Valency undercoordination
   25.6125 !Valency angle/lone pair parameter
    1.0563 !Valency angle
    2.0384 !Valency angle parameter
    6.1431 !Not used
    6.9290 !Double bond/angle parameter
    0.3989 !Double bond/angle parameter: overcoord
    3.9954 !Double bond/angle parameter: overcoord
   -2.4837 !Not used
    4.7747 !Torsion/BO parameter
   10.0000 !Torsion overcoordination
    2.3276 !Torsion overcoordination
   -1.2327 !Conjugation 0 (not used)
    2.1645 !Conjugation
    1.5591 !vdWaals shielding
    0.1000 !Cutoff for bond order (*100)
    2.8921 !Valency angle conjugation parameter
    1.6356 !Overcoordination parameter
    5.6937 !Overcoordination parameter
    2.5067 !Valency/lone pair parameter
    0.5000 !Not used
   20.0000 !Not used
    5.0000 !Molecular energy (not used)
    0.0000 !Molecular energy (not used)
    1.6052 !Valency angle conjugation parameter
  3    ! Nr of atoms; cov.r; valency;a.m;Rvdw;Evdw;gammaEEM;cov.r2;#
            alfa;gammavdW;valency;Eunder;Eover;chiEEM;etaEEM;n.u.
            cov r3;Elp;Heat inc.;n.u.;n.u.;n.u.;n.u.
            ov/un;val1;n.u.;val3,vval4
H     0.6555   1.0000   1.0080   1.6558   0.0228   0.7625  -0.1000   1.0000
     10.0764   4.1572   1.0000   0.0000 116.3988   3.8196   9.8832   1.0000
     -0.1000   0.0000  54.9848   4.0736   2.6883   1.0000   1.0698   0.0000
    -12.5850   2.7466   1.0338   6.2998   2.8793   0.0000   0.0000   0.0000
O     1.1534   2.0000  15.9990   1.7195   0.1292   0.7819   0.9660   6.0000
     10.2695   4.0190   4.0000  32.8323 116.0768   8.5000   7.3000   2.0000
      0.9800   6.8930  -1.1912   2.7851   2.1946   1.0000   0.9745   0.0000
     -6.7189   2.6656   1.0493   6.2998   2.9225   0.0000   0.0000   0.0000
```

```
Si    2.0175    4.0000   28.0600    2.0473    0.1835    0.6587    0.9641    4.0000
     12.3588    1.2523    4.0000   21.7115  139.9309    2.4081    6.4081    0.0000
     -1.0000    0.0000  128.2031    8.7895   23.9298    0.8381    0.8563    0.0000
     -4.7525    2.1607    1.0338    6.2998    2.5791    0.0000    0.0000    0.0000
6       ! Nr of bonds; Edis1;LPpen;n.u.;pbe1;pbo5;13corr;pbo6
                         pbe2;pbo3;pbo4;n.u.;pbo1;pbo2;ovcorr
 1  1 166.5174    0.0000    0.0000   -0.3599    0.0000    1.0000    6.0000    0.6500
        10.6518    1.0000    0.0000    1.0000   -0.0177    5.3255    0.0000
 2  2  81.4891   30.2266  202.3398    0.7334   -0.0688    1.0000   10.4340    0.7000
         1.2986   -0.1057    5.7341    1.0000   -0.1770    5.0269    1.0000
 1  2 217.6778    0.0000    0.0000   -0.7049    0.0000    1.0000    6.0000    0.4031
         4.9325    1.0000    0.0000    1.0000   -0.0668    4.4019    0.0000
 3  3  78.0276   54.0531   30.0000    0.5398   -0.3000    1.0000   16.0000    0.0476
         0.2865   -0.8055    7.1248    1.0000   -0.0681    8.6957    0.0000
 1  3 192.0767    0.0000    0.0000   -0.5621    0.0000    1.0000    6.0000    0.3529
        22.1879    1.0000    0.0000    1.0000   -0.0377    7.2563    0.0000
 2  3 252.6471   53.4022   43.3991   -0.7699   -0.3000    1.0000   36.0000    0.6262
         8.4871   -0.8398   26.9303    1.0000   -0.0982    7.8659    1.0000
3     ! Nr of off-diagonal terms; Ediss;Ro;gamma;rsigma;rpi;rpi2
 1  3    0.0503    1.5421   13.5806    1.3054   -1.0000   -1.0000
 2  3    0.1481    2.0087   11.4016    1.6805    1.4330   -1.0000
 1  2    0.0427    1.7283   10.2714    0.9397   -1.0000   -1.0000
18     ! Nr of angles;at1;at2;at3;Thetao,o;ka;kb;pv1;pv2;val(bo)
 1  1  1    0.0000   27.9213    5.8635    0.0000    0.0000    0.0000    1.0400
 2  2  2   78.4963   61.0192    1.0093  -38.4200    0.4897    0.0000    1.0400
 1  2  2   89.4640   10.1026    4.7764    0.0000    0.0000    0.0000    1.0400
 1  2  1   81.7479   15.4269    4.2247    0.0000    0.0000    0.0000    1.0400
 2  1  2    0.0000    0.0019    6.0000    0.0000    0.0000    0.0000    1.0400
 1  1  2    0.0000    0.0019    6.0000    0.0000    0.0000    0.0000    1.0400
 3  3  3   71.0490   32.4076    1.2648    0.0000    0.0133    0.0000    1.2899
 1  3  3   71.9021   14.1096    1.6768    0.0000    1.6264    0.0000    1.0400
 1  3  1   77.2257   16.0297    2.1560    0.0000    2.8421    0.0000    1.0400
 2  3  3   59.5932   16.1656    0.5837    0.0000    3.5470    0.0000    1.0400
 1  3  2   68.0560   21.3156    4.5715    0.0000    0.5983    0.0000    1.0400
 2  3  2   78.2491   11.8348    0.1760    0.0000    0.4141    0.0000    1.0400
 3  2  3   39.8239    1.2281    0.2412    0.0000    3.7260    0.0000    1.0400
 1  2  3   81.6231    7.6711    4.5986    0.0000    1.4086    0.0000    1.0400
 2  2  3   85.4020   18.1749    1.2713    0.0000    2.6177    0.0000    1.0400
 1  1  3    0.0000   47.1300    6.0000    0.0000    1.6371    0.0000    1.0400
 3  1  3    0.0000   31.5209    6.0000    0.0000    1.6371    0.0000    1.0400
 2  1  3    0.0000   31.0427    4.5625    0.0000    1.6371    0.0000    1.0400
6     ! Nr of torsions;at1;at2;at3;at4;;V1;V2;V3;V2(BO);vconj;n.u;n
 0  1  1  0    0.0000    0.0000    0.0000    0.0000   -1.2327    0.0000    0.0000
 0  1  2  0    0.0000    0.1000    0.0200   -2.5415   -1.2327    0.0000    0.0000
 0  2  2  0    2.6089   -1.7346   -0.1083   -4.7170   -1.2327    0.0000    0.0000
 1  3  3  1    0.0000    0.0000    0.0640   -2.4426    0.0000    0.0000    0.0000
 1  3  3  3    0.0000    0.0000    0.1587   -2.4426    0.0000    0.0000    0.0000
 0  1  3  0    0.0000    0.0000    0.1200   -2.4847    0.0000    0.0000    0.0000
1     ! Nr of hydrogen bonds;at1;at2;at3;Rhb;Dehb;vhb1
 2  1  2    2.1047   -5.2340    3.6501    1.8988
```

REFERENCES

[1] J. A. Walker. "The future of MEMS in telecommunications networks". In: *Journal of Micromechanics and Microengineering* 10.3 (2000), R1–R7.

[2] A. White. *A review of some current research in microelectromechanical systems (MEMS) with defence applications*. Tech. rep. DSTO-GD-0316. DSTO: Weapons Systems Divion, Aeronautical and Maritime Research Laboratory, 2000.

[3] S. Saadon and O. Sidek. "A review of vibration based MEMS piezoelectric energy harvesters". In: *Energy Conversion and Management* 52 (2011), pp. 500–504.

[4] A. C. R. Grayson, R. S. Shawgo, A. M. Johson, N. T. Flynn, Y. Li, M. J. Cima, and R. Langer. "A BioMEMS review: MEMS technology for physiologically integrated devices". In: *Proceedings of the IEEE* 92.1 (), pp. 6–21.

[5] T. Namazu, Y. Isono, and T. Tanaka. "Nano-scale bending test of Si beam for MEMS". In: *The Thirteenth Annual International Conference on Micro Electro Mechanical Systems*. 2000, pp. 205–210.

[6] T. Tsuchiya, O. Tabata, J. Sakata, and Y. Taga. "Specimen size effect on tensile strength of surface micromachined polycrystalline silicon thin films". In: *Journal of Microelectromechanical Systems* 7 (1998), pp. 106–113.

[7] B. L. Boyce. "A sequential tensile method for rapid characterization of extreme-value behavior in microfabricated materials". In: *Experimental mechanics* 50.7 (2010), pp. 993–997.

[8] M. S. Gaither, F. W. DelRio, R. S. Gates, Jr. E. R. Fuller, and R. F. Cook. "Strength distribution of single-crystal silicon theta-like specimens". In: *Scripta Materialia* 63.4 (2010), pp. 422–425.

[9] G. Stan, S. Krylyuk, A. V. Davydov, and R. F. Cook. "Bending manipulation and measurements of fracture strength of silicon and oxidized silicon nanowires by atomic force microscopy". In: *Journal of Materials Research* 27.3 (2012), pp. 562–570.

[10] G. Stan, S. Krylyuk, A. V. Davydov, and R. F. Cook. "Ultimate Bending Strength of Si Nanowires". In: *Nano Letters* 12 (2012), pp. 2599–2604.

[11] Frank W. DelRio, Robert F. Cook, and Brad L. Boyce. "Fracture strength of micro- and nano-scale silicon components". In: *Applied Physics Reviews* 2.2 (June 2015), p. 021303. DOI: 10.1063/1.4919540.

[12] T. Alan, M. A. Hines, and A. T. Zehnder. "Effect of surface morphology on the fracture strength of silicon nanobeams". In: *Applied Physics Letters* 89 (2006), p. 091901.

[13] T. Alan, A. T. Zehnder, D. Sengupta, and M. A. Hines. "Methyl monolayers improve the fracture strength and durability of silicon nanobeams". In: *Applied Physics Letters* 89 (2006), p. 231905.

[14] W. Kern and D. A. Puotinen. "Cleaning solutions based on hydrogen peroxide for use in silicon semiconductor technology". In: *RCA Rev.* 31 (1970), pp. 187–206.

[15] H. J. McSkimin and P. Andreatch. "Elastic moduli of silicon vs hydrostatic pressure at 25.0 °C and -195.8 °C". In: *Journal of Applied Physics* 35.7 (1964), pp. 2161–2165.

[16] R. V CURTIS and R. V CURTIS. "Analysis of strength data using two- and three-parameter Weibull models". In: *Journal of Materials Science* 33.5 (Mar. 1998), pp. 1151–1157. DOI: 10.1023/a:1004361222711.

[17] L. Le Can. "Maximum liklihood: an introduction". In: *International Statistical Review* 58.2 (1990), pp. 153–171.

[18] B. N. Taylor and C. E. Kuyatt. *Guidelines for evaluating and expressing the uncertainty of NIST measurement results*. Tech. rep. 1297. NIST, 1994.

[19] C. Stroh, H. Wang, R. Bash, B. Ashcroft, J. Nelson, H. Gruber, D. Lohr, S. M. Lindsay, and P. Hinterdorfer. "Single-molecule imaging microscopy". In: *PNAS* 101.34 (2004), pp. 12503–12507.

[20] Y. F. Dufrene. "Atomic force microscopy, a powerful tool in microbiology". In: *Journal of Bacteriology* 189.19 (2002), pp. 5205–5213.

[21] B. Bhushan and V. N. Koinkar. "Nanonindentation hardness measurements using atomic force microscopy". In: *Applied Physics Letters* 64 (1994), p. 1653.

[22] *NanoScope V Controller Manual*. Veeco Instruments, Inc.

[23] B. Ohler. *Practical advice on the determination of cantilever spring constants*. Tech. rep. Veeco Instruments Inc, 2007.

[24] T. Alan. "Improving fracture properties of MEMS components by surface control". PhD thesis. Cornell University, 2007.

[25] R. S. Gates and J. R. Pratt. "Prototype cantilevers for SI-traceable nanonewton force calibration". In: *Measurement Science Technology* 17 (2006), pp. 2852–2860.

[26] H. H. Ku. "Notes on the use of propagation of error formulas". In: *Journal of Research of the National Bureau of Standards* 70C.4 (1966), pp. 263–273.

[27] K. Fujii, M. Tanaka, Y. Nezu, A. Sakuma, A. Leistner, and W. Giardini. "Absolute measurement of the density of silicon crystals in vacuo fora determination of the Avagadro constant". In: *IEEE Transactions on Instrumentation and Measurement* 44.2 (1995), pp. 542–525.

[28] A. G. Piersol and T. L. Paez. *Harris' Shock and Vibration Handbook*. 6th ed. McGraw-Hill, 2010.

[29] S. J. Grutzik, R. S. Gates, Y. B. Gerbig, D. T. Smith, R. F. Cook, and A. T. Zehnder. "Accurate spring constant calibration for very stiff atomic force microscopy cantilevers". In: *Review of Scientific Instruments* 84 (2013), p. 113706.

[30] J. R. Pratt, J. A. Kramer, D. B. Newell, and D. T. Smith. "Review of SI traceable force metrology for instrumented indentation and atomic force microscopy". In: *Measurement Science and Technology* 16.11 (2005), pp. 2129–2137.

[31] J. D. Holbery, V. L. Eden, M. Sarikaya, and R. M. Fisher. "Experimental determination of scanning probe microscope cantilever spring constants utilizing a nanoindentation apparatus". In: *Review of Scientific Instruments* 71.10 (2000), p. 3769.

[32] Z. C. Ying, M. G. Reitsma, and R. S. Gates. "Direct measurement of cantilever spring constants and correction for cantilever irregularities using an instrumented indentor". In: *Review of Scientific Instruments* 78 (2007), p. 063708.

[33] C. A. Clifford and M. P. Seah. "Improved methods and uncertainty analysis in the calibration of the spring constant of an atomic force microscope cantilever using static experimental methods". In: *Meas. Sci. Technol.* 20 (2009), p. 125501.

[34] A. Torii, M. Sasaki, K. Hane, and S. Okuma. "A method for determining the spring constant of cantilevers for atomic force microscopy". In: *Meas. Sci. Technology* 7 (1996), pp. 179–184.

[35] C. T. Gibson, G. S. Watson, and S. Myhra. "Determination of the spring constants of probes for force microscopy/spectroscopy". In: *Nanotechnology* 7 (1996), pp. 259–262.

[36] M. Tortonese and M. Kirk. "Characterization of application specific probes for SPMs". In: *SPIE*. Vol. 3009. 1997, pp. 53–60.

[37] R. S. Gates and M. G. Reitsma. "Precise atomic force microscope cantilever spring constant calibration using a reference cantilever array". In: *Review of Scientific Instruments* 78 (2007), p. 086101.

[38] M. S. Kim, J. R. Pratt, U. Brand, and C. W. Jones. "Report on the first international comparison of small force facilities: a pilot study at the micronewton level". In: *Metrologia* 49.1 (2012), p. 70.

[39] D. T. Smith, J. R. Pratt, and L. P. Howard. "A fiber-optic inferometer with subpicometer resolution for DC and low-frequency displacement measurement". In: *Review of Scientific Instruments* 80.3 (2009), p. 035105.

[40] D. Roundy and M. L. Cohen. "Ideal strength of diamond, Si, and Ge". In: *Physical Review B* 64 (2001), p. 212103.

[41] J. P. Boehler. "A simple derivation of representations for non-polynomial constitutive equations in some cases of anisotropy". In: *ZAMM* 59 (1979), pp. 157–167.

[42] Q. S. Zehng and A. J. M. Spencer. "Tensors which characterize anisotropies". In: *International Jounral of Engineering Science* 31.5 (1993), pp. 679–693.

[43] M. F. Salvetti. "Hyperelastic continuum modeling of cubic crystals based on first-principles calculations". PhD thesis. MIT, 2010.

[44] R. L. Liboff. *Introductory Quantum Mechanics*. 4th ed. Addison Wesley, 2003.

[45] E. Engel and R. M. Dreizler. *Density Functional Theory, an Advanced Course*. 1st ed. Springer, 2011.

[46] J. Z. Hu, L. D. Merkle, C. S. Menoni, and I. L. Spain. "Crystal data for high-pressure phases of silicon". In: *Physical Review B* 34.7 (1986), pp. 4679–4684.

[47] S. S. Antman. *Nonlinear problems of elasticity*. 2nd ed. Springer, 2005.

[48] J. J. Boisvert, P. H. Muir, and R. J. Spiteri. *A numerical study of global error and defect control for BVPODEs*. Tech. rep. University of Saskatchewan, 2012.

[49] U. Neuwald, H. E. Hessel, A. Feltz, U. Memmert, and R. J. Behm. "Initial stages of native oxide growth o hydrogen passivated Si(111) surfaces studied by scanning tunneling microscopy". In: *Applied Physics Letters* 60.11 (1992), pp. 1307–1309.

[50] Z. H. Lu, J. P. McCaffrey, B. Brar, G. D. Wilk, R. M. Wallace, L. C. Feldman, and S. P. Tay. "SiO[sub 2] film thickness metrology by x-ray photoelectron spectroscopy". In: *Appl. Phys. Lett.* 71.19 (1997), p. 2764. DOI: 10.1063/1.120438.

[51] T. S. Lassen and S. Tougaard. *QUASES-ARXPS*. 1.1. Tougaard ApS. 2012.

[52] Werner Kern. "Overview and Evolution of Silicon Wafer Cleaning Technology". In: *Handbook of Silicon Wafer Cleaning Technology* (2008), pp. 3–92. DOI: 10.1016/b978-081551554-8.50004-5.

[53] Simon P. Garcia, Hailing Bao, and Melissa A. Hines. "Understanding the pH dependence of silicon etching: the importance of dissolved oxygen in buffered HF etchants". In: *Surface Science* 541.1 (Sept. 2003), pp. 252–261. DOI: 10.1016/s0039-6028(03)00952-x.

[54] R. D. Deslattes *et al. X-ray transition energies*. National Institute of Standards and Technology. Gaithersburg, MD, Apr. 2015.

[55] J. F. Moulder, W. F. Stickle, P. E. Sobol, and K. D. Bomben. *Handbook of X-ray photoelectron spectroscopy*. ULVAC-PHI, 1995.

[56] N. Fairley. *CaxaXPS Manual*. 2.2.15. Casa Software Ltd. 2009.

[57] M. Repoux. "Comparison of background removal methods for XPS". In: *Surface and Interface Analysis* 18.7 (July 1992), pp. 567–569. DOI: 10.1002/sia.740180719.

[58] C. J. Powell and A. Jablonski. *NIST electron inelastic-mean-free-path database*. 1.2. SRD71. Gaithersburg, MD: National Institute of Standards and Technology, Dec. 2010.

[59] S. Tanuma, C. J. Powell, and D. R. Penn. "Calculations of electron inelastic mean free paths (IMFPS). IV. Evaluation of calculated IMFPs and of the predictive IMFP formula TPP-2 for electron energies between 50 and 2000 eV". In: *Surface and Interface Analysis* 20.1 (Jan. 1993), pp. 77–89. DOI: 10.1002/sia.740200112.

[60] S. J. Grutzik, Erik Milosevic, B. L. Boyce, and A. T. Zehnder. "Oxide Driven Evolution of the Strength of Silicon Surfaces". Submitted to Journal of Applied Physics. 2015.

[61] M. Morita, T. Ohmi, E. Hasegawa, M. Kawakami, and M. Ohwada. "Growth of native oxide on a silicon surface". In: *Journal of Applied Physics* 68 (1990), p. 1272.

[62] S. Plimpton. "Fast Parallel Algorithms for Short-Range Molecular Dynamics". In: *Journal of Computational Physics* 117 (1995), pp. 1–19.

[63] A. C. T. van Duin, S. Dasgupta, F. Lorant, and III W. A. Goddard. "ReaxFF: A Reactive Force Field for Hydrocarbons". In: *Journal of Physical Chemistry A* 105.41 (2001), pp. 9396–9409.

[64] M. J. Buehler, A. C. T. van Duin, and III W. A. Goddard. "Multiparadigm Modeling of Dynamical Crack Propagation in Silicon Using a Reactive Force Field". In: *Physical Review Letters* 96 (2006), p. 095505.

[65] A. C. T. van Duin. Personal communication. acv13@psu.edu. Mar. 2012.

[66] A. C. T. van Duin, A. Strachan, S. Stewman, Q. Zhang, x. Xu, and W. A. Goddard III. "ReaxFF Reactive Force Field for Silicon and Silicon Oxide Systems". In: *Journal of Physical Chemistry A* 107 (2003), pp. 3803–3811.

[67] P. Lange, H. Bernt, E. Hartmannsgruber, and F. Naumann. "Growth rate and characterization of silicon oxide films grown in N_2O atmosphere in a rapid thermal processor". In: *Journal of the Electrochemical Society* 141.1 (1994), pp. 259–263.

[68] K. Nakamura, S. Ichimura, A. Kurokawa, K. Koike, G. Inoue, and T. Fukuda. "Ultrathin silicon oxide film grown on Si(100) fabricated by highly concentrated ozone at atmospheric pressure". In: *Journal of Vacuum Science and Technology A* 17 (1999), p. 1275.

[69] F. L. McCrackin, E. Passaglia, R. R. Stromberg, and H. L. Steinberg. "Measurement of the thickness and refractive index of very thin films and the optical properties of surfaces by ellipsometry". In: *Journal of Research of the National Bureau of Standards A* 67A.4 (1963), pp. 363–377.

[70] B. Bhushan, S. P. Murarka, and J. Gerlach. "Stress in silicon dioxide films deposited using chemical vapor deposition techniques and the effect of an-

nealing on these stresses". In: *Journal of Vacuum Science and Tehcnology B* 8 (1990), p. 1068.

[71] *SUMMiT V: Five Level Surface Micromachining Technology Design Manual*. 3.2. Sandia National Laboratories. Oct. 2012.

[72] L. J. Webb, S. Rivillon, D. J. Michalak, Y. J. Chabal, and N. S. Lewis. "Transmission Infrared Spectroscopy of Methyl- and Ethyl-Terminated Silicon(111) Surfaces". In: *The Journal of Physical Chemistry B* 110.14 (Apr. 2006), pp. 7349–7356. DOI: 10.1021/jp054618c.

[73] J. B. Brzoska, I. B. Azouz, and F. Rondelez. "Silanization of solid substrates: A step toward reproducability". In: *Langmuir* 10.11 (1994), pp. 4367–4373.

[74] N. P. Bailey and J. P. Sethna. "Fracture of notched single crystal silicon". arXiv:cond-mat/0301076v1. 2008.